

Robust quantum optimizer with full connectivity

Simon E. Nigg,* Niels Lörch, and Rakesh P. Tiwari

(Dated: August 16, 2021)

Quantum phenomena have the potential to speed up the solution of hard optimization problems. For example quantum annealing, based on the quantum tunneling effect, has recently been shown to scale exponentially better with system size as compared with classical simulated annealing. However, current realizations of quantum annealers with superconducting qubits face two major challenges. First, the connectivity between the qubits is limited, excluding many optimization problems from a direct implementation. Second, decoherence degrades the success probability of the optimization. We address both of these shortcomings and propose an architecture in which the qubits are robustly encoded in continuous variable degrees of freedom. Remarkably, by leveraging the phenomenon of flux quantization, all-to-all connectivity is obtained without overhead. Furthermore, we demonstrate the robustness of this architecture by simulating the optimal solution of a small instance of the NP-hard and fully connected number partitioning problem in the presence of dissipation.

Optimization problems are ubiquitous in nature and throughout human activities such as computational biology, combinatorial chemistry or corporate planning. Consider for example the following task: Given a set of assets with fixed values, is it possible to share them fairly between two parties? This decision problem is an instance of what is known as the Number Partitioning Problem (NPP), which is non-deterministic polynomial-time hard (NP-hard) [1, 2]. This means that any known exact algorithm will take a time exponential in the number of assets to solve at least some instances of this problem. It turns out that this problem, like many others [3], is isomorphic to finding the ground state configuration of an anti-ferromagnetic long range Ising model with free energy

$$E(s_1, s_2, \dots, s_N) = \sum_{ij} J_{ij} s_i s_j, \quad J_{ij} > 0, \quad s_i \in \{-1, 1\}.$$

Finding a ground state means finding a configuration of spins $\{s_1, s_2, \dots, s_N\}$, which minimizes this energy. To map the NPP onto an Ising problem for example, we set $J_{ij} \propto n_i n_j$, where n_i denotes the value of the i -th asset. The Ising spin s_i labels which of the two sets in a given partition of the set of assets $A = F \cup \bar{F}$, the asset i is in. If $s_i = +1$ then the asset is in F , while if $s_i = -1$ the asset is in the complement $\bar{F} = A \setminus F$. A fair partition exists if and only if the corresponding ground state energy is zero since then: $\sum_{i \in F} n_i = \sum_{i \in \bar{F}} n_i$. If no fair partition exists, minimizing the energy will yield the least unfair partition.

It is noteworthy that for the NPP approximate solutions obtained via classical heuristics, such as simulated annealing [4], can be very poor [5]. In general, the optimization landscapes of hard problems are typically highly non-convex and heuristic approaches tend to get trapped in local minima. In 1998, Kadowaki and Nishimori [6], introduced the idea that the phenomenon of quantum tunneling could help to escape from local potential minima. This insight and subsequent works [7–9] have led to high interest in quantum annealing both in academia and in the private sector [10–14]. While a genuine quantum speedup over the best known classical heuristic algorithms remains to be demonstrated, there are strong indications that this could be achieved in the near future. In par-

ticular, for problem instances with high and narrow barriers, the D-wave quantum annealer [15] has been shown to succeed exponentially faster than thermally activated simulated annealing.

TWO MAIN CHALLENGES

Many hard optimization problems map onto Ising models with dense connectivity graphs. The D-wave architecture however has limited connectivity [15]. This is due to the fact that the interconnections between qubits are realized by physical coupler devices. Because the number of connections grows quadratically with the number of qubits, such an approach quickly represents an intractable design challenge. To circumvent this connectivity problem, the standard approach is to use a minor embedding (ME) scheme [16, 17] to map a fully connected graph onto the sparse physical graph. However, this comes at the cost of a substantial overhead in the number of physical qubits. More recently another mapping was proposed, where instead of the N bits of the Ising model, the $N(N-1)/2$ binary pairings are encoded in a two-dimensional lattice of qubits with four-qubit nearest neighbor interactions [18]. Implementations of this idea with superconducting circuits have been proposed in Refs. [19] and [20]. Also in this case there remains a substantial overhead as compared to a direct implementation. In contrast, here we propose a superconducting continuous variable Ising machine (CVIM) with full connectivity and zero overhead, paving the way to experimentally demonstrate quantum supremacy [21].

Ideally, quantum annealing relies on the coherent evolution of the ground state of an isolated quantum system, the Hamiltonian of which is varied in time adiabatically [22]. Typically, the Ising spin s_i is encoded in the two states of a qubit and the Hamiltonian is of the form (we set $\hbar = 1$)

$$H_A(t) = \varepsilon(t) \sum_j \sigma_j^x + H_{\text{Ising}}. \quad (1)$$

The value of the control parameter $\varepsilon(t)$ is initially chosen such that $|\varepsilon(t=0)| \gg \max |J_{ij}|$ and the system is prepared in the ground state of $H_A(0)$. ε is then gradually reduced to zero

such that $\mathbf{H}_A(T) = \mathbf{H}_{\text{Ising}} = \sum_{ij} J_{ij} \sigma_i^z \sigma_j^z$. If the adiabatic condition is satisfied [22], the system at time T is in the ground state of the quantum Ising model. Real world quantum annealers however are open quantum systems. It was recognized early on that one of the potential strengths of quantum annealing is its relative robustness to certain types of errors affecting the underlying qubits [23–27]. More precisely, if decoherence takes place only in the instantaneous energy eigenbasis of (1), then it does not decrease the success probability of the optimization as compared with the coherent limit [23]. In general however, decoherence takes place in different channels depending on the physical hardware. Dephasing errors in the Ising basis for example, described by the random action of σ_j^z operators, are deleterious to the success of the optimization, because the error operators do not commute with the transverse part of the Hamiltonian (1) and hence lead to transitions out of the ground state in the initial stages of the annealing process [13]. In contrast, here we show that quantum annealing with our continuous variable system is remarkably robust to decoherence. A key result of the present work is that if the annealing rate is below the problem specific adiabatic threshold but large compared with the dissipation rate, then a single run of the continuous variable optimizer will succeed with probability > 0.5 for ramp rates smaller than but arbitrarily close to the threshold value.

CONTINUOUS VARIABLE ISING MACHINE

The binary Ising spin variable s_i is encoded into the quantized phase of a Kerr parametric oscillator [28–33] (KPO) above threshold, which can take on two values: 0, corresponding to $s_i = +1$ or π , corresponding to $s_i = -1$. The dynamics of such a system is described by the Hamiltonian

$$\mathbf{H}_a(\Delta, K) = \Delta \mathbf{a}^\dagger \mathbf{a} + \varepsilon (\mathbf{a}^2 + \mathbf{a}^{\dagger 2}) - K \mathbf{a}^\dagger \mathbf{a}^\dagger \mathbf{a} \mathbf{a}.$$

Here \mathbf{a} and \mathbf{a}^\dagger are bosonic annihilation and creation operators, $K > 0$ is the strength of the Kerr nonlinearity and ε is the strength of a two-photon drive. If $\Delta < 0$, then at $\varepsilon = 0$ the vacuum is the ground state of the system. As the drive strength is increased, the system undergoes a bifurcation at the threshold value $\varepsilon_{\text{th}} = |\Delta|$ into a superposition of coherent states $(|\alpha\rangle + |-\alpha\rangle)/\sqrt{2}$ with $\alpha \simeq \sqrt{\varepsilon/K}$, also called a cat state.

In Ref. [31, 32], a system of N KPOs, coupled via a term of the form $\sum_{nm} J_{nm} \mathbf{a}_n^\dagger \mathbf{a}_m$ was considered. It was shown, using perturbation theory, that as the two photon drive strength of each KPO is varied from $\varepsilon = 0$ to $\varepsilon \gg |\Delta|$, the multi-mode vacuum $|0_1, 0_2, \dots, 0_N\rangle$ is adiabatically connected to a multi-mode cat state of the form

$$\frac{1}{\sqrt{2}} (|s_1 \alpha, s_2 \alpha, \dots, s_N \alpha\rangle + |-s_1 \alpha, -s_2 \alpha, \dots, -s_N \alpha\rangle), \quad (2)$$

where $s_1, \dots, s_N \in \{-1, 1\}$ are such that the Ising energy $-\sum_{n,m} J_{nm} s_n s_m$ is minimized. Such a system thus presents the opportunity to encode an Ising optimization problem in the

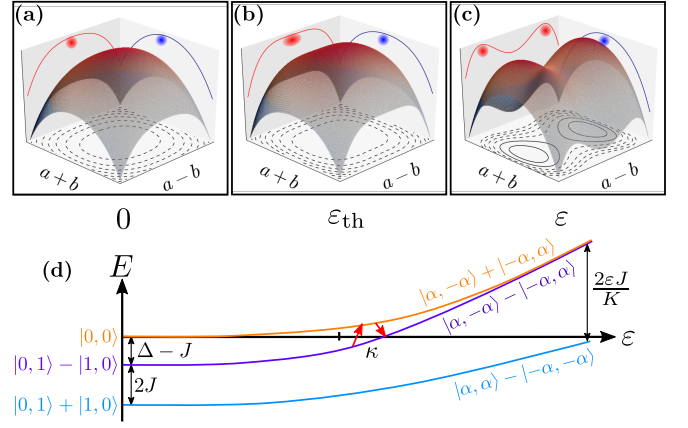


FIG. 1. Illustration of the bifurcation-based annealing process in two anti-ferromagnetically coupled KPOs. Panels (a), (b) and (c) show the evolution of the 2D energy landscape with increasing two-photon drive strength ε . Shown is the anti-ferromagnetic case ($J < 0$), where the anti-symmetric mode $\mathbf{a} - \mathbf{b}$ is softer, and thus has a lower bifurcation threshold, than the symmetric mode $\mathbf{a} + \mathbf{b}$. Consequently, the system evolves from the vacuum $|0,0\rangle$ at $\varepsilon = 0$ to the two-mode cat state $|\phi_+\rangle = (|\alpha, -\alpha\rangle + |-\alpha, \alpha\rangle)/\sqrt{2}$ at large ε , as shown in panel (d). Photon loss events predominantly take place above threshold and induce transitions between the cat states $|\phi_+\rangle$ and $|\phi_-\rangle = (|\alpha, -\alpha\rangle - |-\alpha, \alpha\rangle)/\sqrt{2}$, as indicated by the red arrows in panel (d).

adiabatic dynamics of a continuous variable quantum system. To build some intuition we consider first the simple case of two identical coupled KPOs and denote their operators with \mathbf{a} and \mathbf{b} . The mutual coupling then has the form $J(\mathbf{a}^\dagger \mathbf{b} + \mathbf{b}^\dagger \mathbf{a})$. In the weakly nonlinear limit $K \ll 4|J|$, the Hamiltonian of this system can be conveniently written in the basis of the symmetric $\mathbf{d} = (\mathbf{a} + \mathbf{b})/\sqrt{2}$ and anti-symmetric $\mathbf{c} = (\mathbf{a} - \mathbf{b})/\sqrt{2}$ modes as (see Methods)

$$\mathbf{H}_2 = \mathbf{H}_d(\Delta + J, K/2) + \mathbf{H}_c(\Delta - J, K/2) - K \mathbf{d}^\dagger \mathbf{d} \mathbf{c}^\dagger \mathbf{c}.$$

This corresponds to two KPOs with *different* frequencies, coupled via a *cross*-Kerr term $-K \mathbf{d}^\dagger \mathbf{d} \mathbf{c}^\dagger \mathbf{c}$. If $\Delta \pm J < 0$, then the two-mode vacuum $|0,0\rangle$ is the ground state. Because of the different frequencies the thresholds of the two modes are shifted to $|\Delta + J|$ for the symmetric mode and to $|\Delta - J|$ for the anti-symmetric mode. Hence, as the two-photon drive strength of the two KPOs is increased, the soft mode (\mathbf{d} if $J > 0$ and \mathbf{c} if $J < 0$), undergoes a bifurcation before the hard mode (\mathbf{c} if $J > 0$ and \mathbf{d} if $J < 0$). Importantly, once the soft mode starts to bifurcate and becomes populated with photons, the cross-Kerr coupling makes the hard mode even harder, pushing its bifurcation threshold further away. Hence, the Kerr nonlinearity provides a stabilizing feedback mechanism. This is schematically illustrated in Fig. 1 (a-c).

PHYSICAL IMPLEMENTATION

We next turn to the physical implementation of such a machine with superconducting circuits. Prototypes of similar bifurcation based coherent Ising machines have been built with optical systems [34–36]. Up until now however, no physical realization has been proposed that implements a dense connectivity graph in a scalable fashion. As compared with optical systems, superconducting Josephson circuits offer the crucial advantage of stronger nonlinearities that have recently reached the quantum regime, where the nonlinear frequency shifts are larger than the resonance linewidths [37–39].

A single KPO can be engineered with superconducting circuits by modulating the flux through a split Josephson junction (Fig. 2) at close to twice its natural resonance frequency [30, 33]. The Kerr nonlinearity is provided by the Josephson potential expanded to fourth order in a regime where the Josephson energy exceeds the charging energy.

While several superconducting KPOs can be coupled inductively, this typically yields only a short range interaction between nearest neighbors. Long range coupling between all pairs of N oscillators can however be obtained if the oscillators are connected in series and shunted by an inductive element as shown in Fig. 2. Indeed, flux quantization imposes a constraint on the sum of all phase drops across the KPOs ($\{\varphi_n\}_{n=1,\dots,N}$) and across the shunt (φ_0) such that $\varphi_0 = \sum_{n=1}^N \varphi_n$. The inductive energy of the shunt

$$\frac{\varphi_0^2}{2L_{\text{eff}}} = \frac{1}{2L_{\text{eff}}} \left(\sum_{n=1}^N \varphi_n^2 + \sum_{n \neq m} \varphi_n \varphi_m \right),$$

then immediately yields an interaction term between all KPOs. After including the capacitive energies and proceeding with standard circuit quantization [40], $\varphi_n \rightarrow \sqrt{Z_n/2}(\mathbf{a}_n + \mathbf{a}_n^\dagger)$, where Z_n denotes the mode impedance, we obtain [30] the effective Hamiltonian in a frame rotating with half the ac flux modulation frequencies $\Omega_n = 2(\omega_n - \Delta)$

$$\begin{aligned} H_N = & \Delta \sum_{n=1}^N \mathbf{a}_n^\dagger \mathbf{a}_n + \sum_{n=1}^N \varepsilon_n (\mathbf{a}_n^2 + \mathbf{a}_n^{\dagger 2}) \\ & + \sum_{n \neq m} J_{nm} e^{i(\omega_n - \omega_m)t} \mathbf{a}_n^\dagger \mathbf{a}_m - \sum_{n=1}^N K_n \mathbf{a}_n^\dagger \mathbf{a}_n^\dagger \mathbf{a}_n \mathbf{a}_n. \end{aligned} \quad (3)$$

Here $\omega_n \simeq 4\sqrt{E_C^{(n)} E_J^{(n)} \cos(\Phi_n^{\text{dc}})}$ is the natural frequency of the n -th KPO expressed in terms of the charging and Josephson energies [40] of the Josephson junctions $E_C^{(n)}$ and $E_J^{(n)}$ and the dc part of the flux bias Φ_n^{dc} . The two photon drive strength is $\varepsilon_n \simeq (E_J^{(n)}/4)Z_n \sin(\Phi_n^{\text{dc}})\delta\Phi_n^{\text{ac}}$, where $Z_n = 8E_C^{(n)}/\omega_n$ and $\delta\Phi_n^{\text{ac}}$ is the strength of the ac flux modulation at frequency Ω_n . We have assumed $|\Delta| \ll \omega_n$ and applied the rotating wave approximation to suppress fast rotating terms. In the regime $E_J^{(n)} \gg E_C^{(n)}$, the strength of the Kerr nonlinearity of oscillator n is $K_n \simeq E_C^{(n)}/2$ and finally, the interaction strength between oscillators n and m is $J_{nm} \simeq \sqrt{Z_n Z_m}/(2L_{\text{eff}})$. In order to

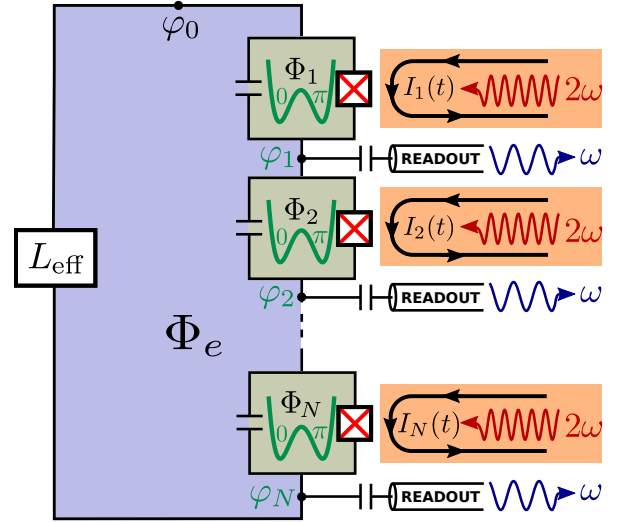


FIG. 2. Schematics of the proposed superconducting continuous variable Ising machine (CVIM). It consists of a chain of split Josephson junctions shunted by an effective inductor L_{eff} . An ac modulation of the flux bias through the split junction loops at twice their resonance frequency turns them into KPOs with a pitchfork bifurcation (indicated by the double well potentials). The Ising spin variables are encoded in the quantized oscillation phases (either 0 or π) of these oscillators above threshold. An effective inductive shunt induces all-to-all coupling between the KPOs. In order to obtain anti-ferromagnetic coupling, a large area Josephson junction can be used as a shunt together with a flux bias of $\Phi_e = \Phi_0/2$. Homodyne readout of the oscillator phases is enabled via capacitively coupled transmission lines [30].

achieve all-to-all coupling, the N KPOs must be made resonant with each other. This can be achieved by tuning the N dc flux biases Φ_n^{dc} such that $\omega_1 \simeq \omega_2 \simeq \dots \simeq \omega_N$. Note that if the shunt is a conventional inductor, the coupling strengths so far are all positive, implying that only ferromagnetic instances of the Ising model can be accessed. While some non-trivial optimization problems can be mapped onto ferromagnetic Ising models with inhomogeneous longitudinal fields [13], others such as the NPP require anti-ferromagnetic couplings. Moreover, anti-ferromagnetic couplings can give rise to frustration that is intimately related to spin glass physics [10, 41]. Anti-ferromagnetic coupling can be achieved by substituting the shunt inductor with a large area Josephson junction and by biasing the loop created by the N KPOs and the shunt with half a flux quantum (see Methods). Under the condition that $NE_J^{(0)} < E_J^{(n)}$, where $E_J^{(0)}$ denotes the Josephson energy of the shunt junction, the latter effectively acts as a *negative* inductor and the coupling matrix elements become [30] $J_{nm} \simeq -(E_J^{(0)}/2)\sqrt{Z_n Z_m}$. We remark that a π -junction [42–44] shunt, provides an alternative to realize anti-ferromagnetic couplings. Tunability of the matrix elements is enabled by connecting a tunable capacitor in parallel with the split junction of each KPO. While tunable high-Q capacitors in the microwave regime are not yet part of the standard toolbox of cQED, their development is an active area of research [45, 46].

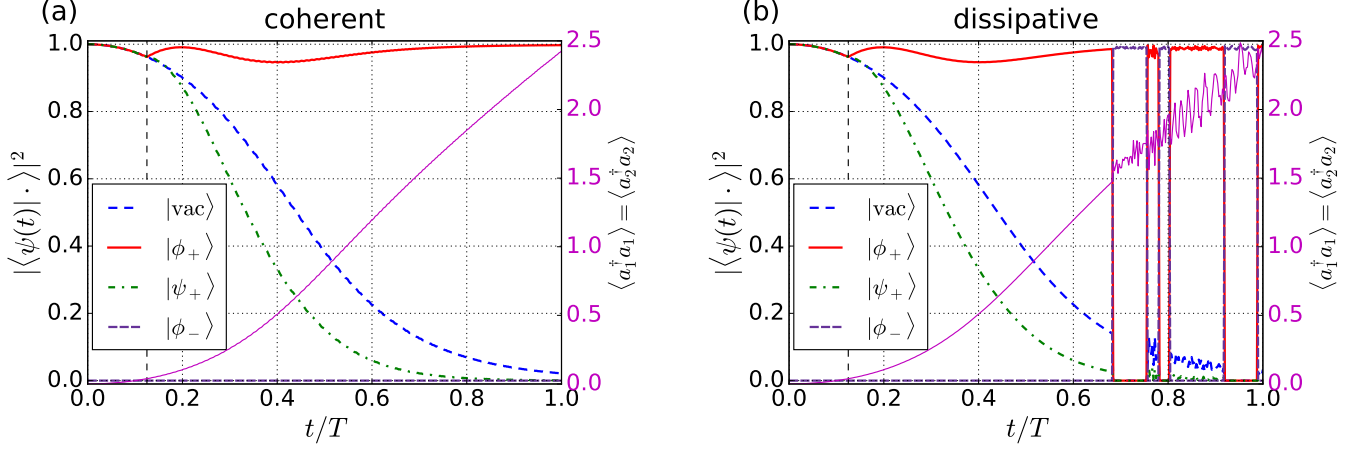


FIG. 3. Comparison between coherent and dissipative quantum annealing for two anti-ferromagnetically coupled equal KPOs. The state $|\psi(t)\rangle$ is obtained by numerically solving the Schrödinger equation with Hamiltonian (3). Shown are the fidelities with respect to the vacuum $|\text{vac}\rangle = |0, 0\rangle$ as well as the three states $|\phi_{\pm}\rangle = (|\alpha, -\alpha\rangle \pm |-\alpha, \alpha\rangle)/\sqrt{2}$ and $|\psi_{\pm}\rangle = (|\alpha, \alpha\rangle + |-\alpha, -\alpha\rangle)/\sqrt{2}$. The amplitude α is given by Eq. (5). (a) Without dissipation: $\kappa = 0$. The system evolves from the vacuum $|\text{vac}\rangle = |0\rangle|0\rangle$ (dashed blue line) at $t = 0$ to the even parity cat state $|\phi_{+}\rangle$ (full red line) at $t = T$. The latter state encodes the ground state of the corresponding anti-ferromagnetic Ising model ($J < 0$). The population of the odd photon number parity state $|\phi_{-}\rangle$ remains zero (dashed purple line). The bifurcation dynamics is clearly visible as a kink of the population of $|\phi_{+}\rangle$, when the drive strength reaches the threshold value $\varepsilon_{\text{soft}} = \frac{1}{2}\sqrt{(\Delta + |J|)^2 + \left(\frac{\kappa}{2}\right)^2}$ (vertical thin dashed black line). (b) With dissipation: $\kappa = 0.01$ MHz. Shown is a quantum trajectory with six jumps obtained from a Monte Carlo simulation of the dissipative dynamics. A photon loss event induces a transition between the even and odd photon number parity cat states. Note however, that both $|\phi_{+}\rangle$ and $|\phi_{-}\rangle$ encode correctly the anti-ferromagnetic Ising spin correlations. Also note the absence of jumps below threshold, where the average photon number (thin magenta line) is close to zero. The parameter values used in both simulations are: $\Delta = -1$ MHz, $J = -0.5$ MHz, $K = 0.7$ MHz, $T = 400 \mu\text{s}$, $\varepsilon_{\text{MAX}} = 2.0$ MHz and $\varepsilon(t) = \varepsilon_{\text{MAX}}(t/T)$.

Even without this tunability, a proof-of principle experiment is within reach of current technology.

ROBUSTNESS TO DISSIPATION

The dominant decoherence source in this system is energy dissipation that occurs due to internal losses in the device or via the capacitively coupled readout lines (see Fig. 2 and [30]). We describe this dissipation by including photon losses with rate κ using a standard Lindblad master equation

$$\dot{\rho} = -i(\mathbf{H}_{\text{NH}}\rho - \rho\mathbf{H}_{\text{NH}}) + \kappa \sum_{n=1}^N \mathbf{a}_n \rho \mathbf{a}_n^{\dagger}. \quad (4)$$

Here $\mathbf{H}_{\text{NH}} = \mathbf{H}_N - i\frac{\kappa}{2} \sum_{n=1}^N \mathbf{a}_n^{\dagger} \mathbf{a}_n$ and \mathbf{H}_N is given by Eq. (3). This way of writing the master equation emphasizes the two different aspects of photon loss: The first term on the right hand side represents a non-unitary but deterministic evolution of the state, while the second term on the right hand side represents the stochastic, i.e. non-deterministic “jump” action of an annihilation operator on the state [47].

A key property of the continuous variable Ising encoding is its robustness to photon loss. This robustness can be illustrated with the simple case of two coupled identical KPOs (see Fig. 1). The dissipation modifies the thresholds of the soft

and hard modes [30] as $\varepsilon_{\text{soft/hard}} = \frac{1}{2}\sqrt{(\Delta \pm |J|)^2 + \left(\frac{\kappa}{2}\right)^2}$. If the drive strength is varied adiabatically, then under the action of \mathbf{H}_{NH} , the wavefunction of the system splits deterministically into an equal superposition between the two maxima of the potential to remain in the instantaneous steady state [48]. Note that this evolution preserves the purity of the state. In the original basis then, the two-mode vacuum evolves into a two-mode cat state with even photon number parity (see Fig. 3 (a)):

$$|0, 0\rangle \rightarrow \begin{cases} (|\alpha, \alpha\rangle + |-\alpha, -\alpha\rangle)/\sqrt{2}, & \text{for } J > 0, \\ (|\alpha, -\alpha\rangle + |-\alpha, \alpha\rangle)/\sqrt{2}, & \text{for } J < 0. \end{cases}$$

Far above threshold, the amplitude can be found from the solution of the semi-classical equations of motion (see Methods)

$$\alpha = e^{i\phi} \sqrt{\frac{\sqrt{4\varepsilon^2 - \left(\frac{\kappa}{2}\right)^2} + \Delta + |J|}{2K}}, \quad (5)$$

with $\phi = -\frac{1}{2} \arctan\left[\frac{\kappa}{\sqrt{16\varepsilon^2 - \kappa^2}}\right]$.

Let us now turn to the jump part of the dissipative process (see Eq. (4)). Below threshold, the average photon number \bar{n} is low (see Fig. 3). Therefore, the probability of a photon loss event below threshold is strongly suppressed and consequently the impact of dissipation on the annealing process is reduced. Above threshold, the

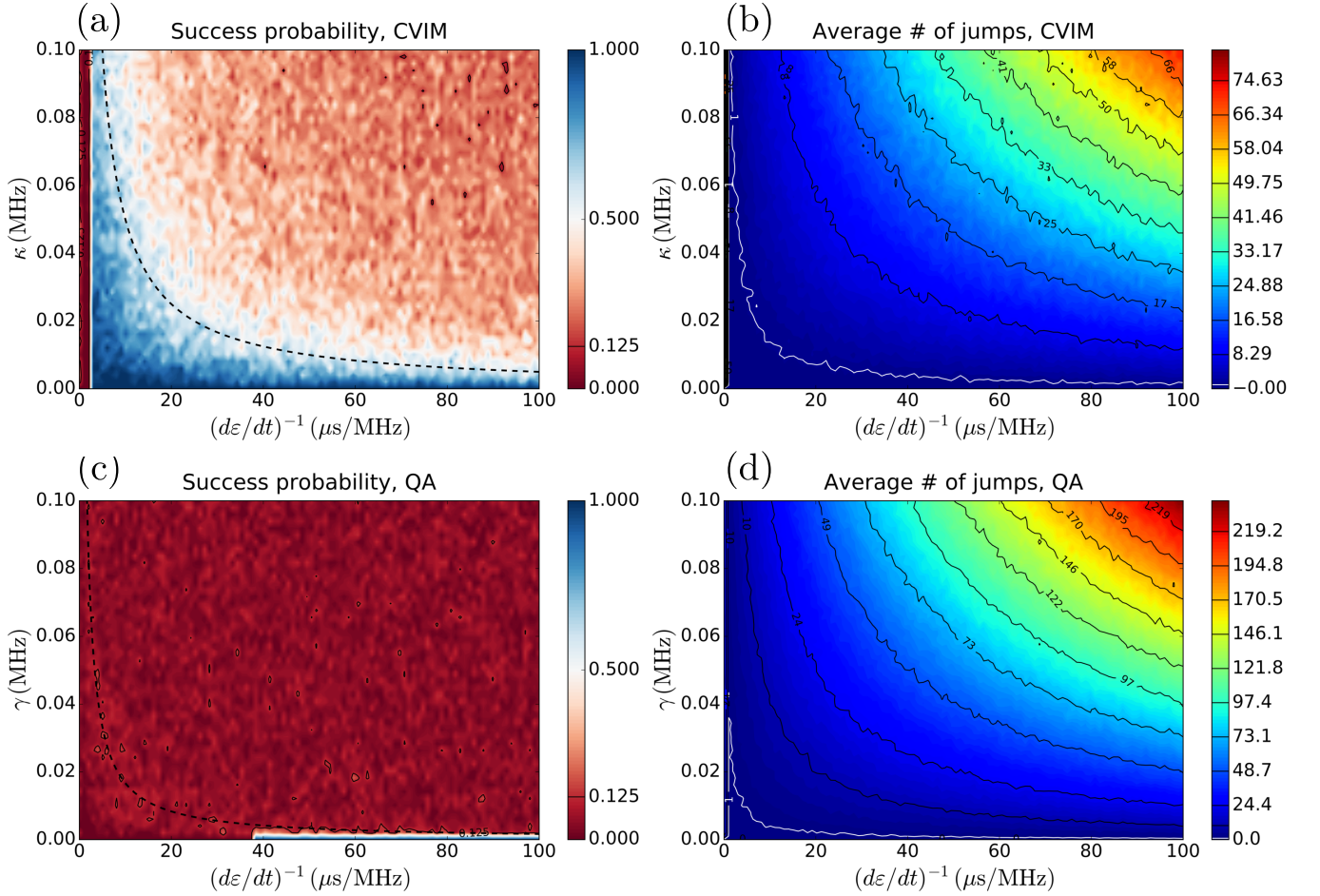


FIG. 4. Comparison of performance between the continuous variable Ising machine (CVIM) ((a) and (b)) and a standard discrete qubit based quantum annealer (QA) ((c) and (d)). Panels (a) and (c) show the success probability of the number partitioning problem with set $S = \{4, 5, 6, 7\}$ as a function of the ramp rate $d\varepsilon/dt$ and the photon loss rate κ in (a) or dephasing rate γ in (c). Panels (b) and (d) show the corresponding mean number of jump events (photon loss for (b) and dephasing events for (d)). While the success probability of the QA drops sharply already after a single (on average) dephasing event (see region within white contour in panel (d)), the CVIM still succeeds with probabilities > 0.5 even when more than one photon has been lost (see region within the white contour in panel (b)). Also, the adiabatic ramp rate threshold for the CVIM is substantially higher than for the QA. Finally, the success probability for the CVIM is typically above that for a random guess $\sim 1/8 = 0.125$, in the entire region shown above the adiabatic threshold, while the success probability of the QA quickly drops below the random guess value delimited by thin solid black contour lines in (a) and (c). The parameter values for the CVIM simulations (a) and (b) are: $\Delta = -1.5$ MHz, $K = 0.6$ MHz, $\varepsilon_{\text{MAX}} = 2$ MHz and $\varepsilon(t) = \varepsilon_{\text{MAX}}(t/T)$ for T in the range $(0, 200)$ μs . The parameters for the QA simulations (c) and (d) are: $\varepsilon(t) = \varepsilon_{\text{MAX}}(1 - t/T)$ with $\varepsilon_{\text{MAX}} = 6$ MHz and T in the range $(0, 600)$ μs . The dashed black curves in (a) and (c) indicate the points where $\kappa T = 1$ respectively $\gamma T = 1$. Each point in all figures corresponds to an average over 40 trajectories.

jumps lead to the random switching of the photon number parity (Fig. 3 (b)). In the ensemble averaged picture this results in dephasing of the pure states into mixtures of two-mode coherent states i.e., $(|\alpha, \alpha\rangle + |-\alpha, -\alpha\rangle)/\sqrt{2} \xrightarrow{a,b} (|\alpha, \alpha\rangle\langle\alpha, \alpha| + |-\alpha, -\alpha\rangle\langle-\alpha, -\alpha|)/2$, as well as $(|\alpha, -\alpha\rangle + |-\alpha, \alpha\rangle)/\sqrt{2} \xrightarrow{a,b} (|\alpha, -\alpha\rangle\langle\alpha, -\alpha| + |-\alpha, \alpha\rangle\langle-\alpha, \alpha|)/2$. Crucially though, photon loss above threshold, does not corrupt the Ising spin correlations, i.e. for $J > 0$ ($J < 0$), the two oscillators still oscillate in-phase (with opposite phase) (Figs. 1 (d) and 3). This robustness of the annealing process to dissipation, is to be contrasted with a conventional discrete qubit based implementation of a quantum annealer, where initially

the state of the annealer is a fragile coherent superposition of all possible spin configurations and the impact of qubit dephasing in the Ising basis before the avoided crossing strongly reduces the population of the ground state [13, 30].

APPLICATION TO NUMBER PARTITIONING

To demonstrate the capabilities of our proposed device, we have simulated an instance of the NPP with $N = 4$ oscillators using a Monte Carlo quantum trajectory algorithm [49]. The NPP is defined by the set $A = \{4, 5, 6, 7\}$, for which a fair partition is $F = \{4, 7\}$ and $\bar{F} = \{5, 6\}$. To encode the

corresponding Ising problem into our circuit we set the coupling matrix elements as $J_{ij} = -J_0 A_i A_j$ and $J_{ii} = 0$. Here $J_0 > 0$ is a scale factor that leaves the Ising problem invariant and which is convenient to satisfy the physical constraints on the coupling strengths. We choose $J_0 = 1/\max|J_{ij}| = 1/42$. The two Ising spin configurations that satisfy this NPP are $\{s_1 = s_4 = 1, s_2 = s_3 = -1\}$, and the configuration with all spins flipped. Fig. 4 (a) shows the success probability as a function of $(d\varepsilon/dt)^{-1} = T/\varepsilon_{\text{MAX}}$ and the photon loss rate κ . Fig. 4 (b) shows the corresponding average number of jump events. Each point in both figures represents an average over 40 trajectories. A particular run of the optimizer is deemed successful if the phase correlations between each pair of oscillators, as measured by $\text{sign}\{\cos(\arg[\langle a_i^\dagger a_j \rangle])\}$, is equal to $s_i s_j$, at the final drive strength value ε_{MAX} . For comparison, Fig. 4 (c) shows the success probability, obtained for the same NPP, when simulating a standard quantum annealer consisting of four qubits that are subject to dephasing with rate γ in the basis that diagonalizes the Ising terms. Clearly, the optimization in the CVIM is more robust. Success probabilities above 0.5 are obtained even when the average number of photons lost during the annealing is larger than one (Fig. 4 (b)). In contrast, the optimization with the spin-based quantum annealer fails already after a single dephasing event (Fig. 4 (d)). This can be understood by observing that in the initial state of the annealer, where the spins are polarized along σ_i^x for $i \in \{1, 2, 3, 4\}$, a dephasing error described by σ_i^z induces transitions out of the ground state to excited states that are not adiabatically connected with the solution of the optimization problem [30].

In conclusion, we have proposed and investigated both analytically and numerically the implementation of a quantum Ising optimization machine with superconducting circuits, which solves two of the major challenges in the field. First, we show that flux quantization enables the realization of all-to-all connectivity among the Ising spins, without overhead, i.e., N oscillators are sufficient to encode N Ising spins with full connectivity. Second, we show that with this continuous variable encoding of the Ising minimization problem, quantum annealing succeeds with high probability in a dissipative regime with high error rate where conventional discrete qubit based quantum annealing breaks down. Our results open up new perspectives for quantum optimization.

Acknowledgments The numerical calculations were performed in a parallel computing environment at sciCORE (<http://scicore.unibas.ch/>) scientific computing core facility at University of Basel. S. E. N. acknowledges financial support from the Swiss NSF. R. P. T. was financially supported by the Swiss SNF and the NCCR Quantum Science and Technology.

Author contributions S. E. N. developed the concepts, carried out the calculations, wrote the numerical code and the manuscript and contributed to the interpretation of the results. R. P. T. contributed to the calculations, the interpretation of the results and the manuscript and N. L. contributed to the numerics, the interpretation of the results and the manuscript.

METHODS

Two coupled KPOs

The Hamiltonian of two coupled KPOs in the basis of the symmetric/anti-symmetric modes d and c reads

$$K(a^\dagger a^\dagger aa + b^\dagger b^\dagger bb) = \frac{K}{2}(d^\dagger d^\dagger dd + c^\dagger c^\dagger cc) + Kd^\dagger dc^\dagger c + \frac{K}{2}(d^\dagger d^\dagger cc + c^\dagger c^\dagger dd).$$

Given that the frequency of the symmetric/anti-symmetric modes are $\Delta \pm J$, the terms on the second line rotate with frequency $2J$ and if $K \ll 4|J|$ they can be neglected in rotating wave approximation.

Semi-classical equations of motion

The semi-classical equations of motion are obtained by replacing the quantum operators a and b by complex functions in the Heisenberg-Langevin equations of motion. They read

$$i\dot{\alpha} = (\Delta - 2K|\alpha|^2)\alpha + J\beta + 2\varepsilon\alpha^* - i\frac{\kappa}{2}\alpha, \\ i\dot{\beta} = (\Delta - 2K|\beta|^2)\beta + J\alpha + 2\varepsilon\beta^* - i\frac{\kappa}{2}\beta.$$

A linear stability analysis of the solutions of these equations is provided in Ref. [30].

Anti-ferromagnetic coupling

The potential energy of the system with a large area Josephson junction shunt and a half-flux quantum flux bias $\Phi_e = \Phi_0/2$ is

$$\mathcal{U} = E_J^{(0)} \cos\left(\sum_{n=1}^N \varphi_n\right) - \sum_{n=1}^N E_J^{(n)} \cos(\varphi_n).$$

For small oscillations, the potential minimum satisfies the transcendental equation [30]

$$\varphi_n \simeq \frac{E_J^{(0)}}{E_J^{(n)}} \sin(N\varphi_n).$$

When $NE_J^{(0)} < E_J^{(n)}$, the only solution of this equation is $\varphi_n = 0$. Expanding the shunt potential around this classical minimum and quantizing yields the anti-ferromagnetic interaction term given in the main text [30].

* Corresponding author: simon.nigg@unibas.ch

- [1] M. R. Garey and D. S. Johnson, *Computers and Intractability: A Guide to the Theory of NP-Completeness* (W. H. Freeman, New York, 1997).
- [2] S. Mertens, Phys. Rev. Lett. **81**, 4281 (1998).
- [3] A. Lucas, Frontiers in Physics **2**, 5 (2014).
- [4] S. Kirkpatrick, C. D. Gelatt, and M. P. Vecchi, Science **220**, 671 (1983).
- [5] B. Hayes, American Scientist **90**, 113 (2002).
- [6] T. Kadowaki and H. Nishimori, Phys. Rev. E **58**, 5355 (1998).
- [7] J. Brooke, D. Bitko, R. T.F., and G. Aeppli, Science **284**, 779 (1999).
- [8] Y.-H. Lee, , and B. J. Berne, The Journal of Physical Chemistry A **104**, 86 (2000).
- [9] E. Farhi, J. Goldstone, S. Gutmann, J. Lapan, A. Lundgren, and D. Preda, Science **292**, 472 (2001).
- [10] G. E. Santoro, R. Martoňák, E. Tosatti, and R. Car, Science **295**, 2427 (2002).
- [11] M. W. Johnson, M. H. S. Amin, S. Gildert, T. Lanting, F. Hamze, N. Dickson, R. Harris, A. J. Berkley, J. Johansson, P. Bunyk, et al., Nature **473**, 194 (2011).
- [12] S. Boixo, T. F. Ronnow, S. V. Isakov, Z. Wang, D. Wecker, D. A. Lidar, J. M. Martinis, and M. Troyer, Nat Phys **10**, 218 (2014).
- [13] S. Boixo, V. N. Smelyanskiy, A. Shabani, S. V. Isakov, M. Dykman, V. S. Denchev, M. H. Amin, A. Y. Smirnov, M. Mohseni, and H. Neven, Nat Commun **7** (2016).
- [14] C. Neill, P. Roushan, M. Fang, Y. Chen, M. Kolodrubetz, Z. Chen, A. Megrant, R. Barends, B. Campbell, B. Chiaro, et al., Nat Phys **advance online publication** (2016), letter.
- [15] V. S. Denchev, S. Boixo, S. V. Isakov, N. Ding, R. Babbush, V. Smelyanskiy, J. Martinis, and H. Neven, Phys. Rev. X **6**, 031015 (2016).
- [16] V. Choi, Quantum Information Processing **7**, 193 (2008).
- [17] V. Choi, Quantum Information Processing **10**, 343 (2011).
- [18] W. Lechner, P. Hauke, and P. Zoller, Science Advances **1** (2015).
- [19] M. Leib, P. Zoller, and W. Lechner, arXiv:1604.02359 (2016).
- [20] P. A. W. Nicholas Chancellor, Stefan Zohren, arXiv:1603.09521 (2016).
- [21] S. Boixo, S. V. Isakov, V. N. Smelyanskiy, R. Babbush, N. Ding, Z. Jiang, J. M. Martinis, and H. Neven, arXiv:1608.00263 (2016).
- [22] M. Born and V. Fock, Zeitschrift für Physik **51**, 165 (1928).
- [23] A. M. Childs, E. Farhi, and J. Preskill, Phys. Rev. A **65**, 012322 (2001).
- [24] M. S. Sarandy and D. A. Lidar, Phys. Rev. Lett. **95**, 250503 (2005).
- [25] J. Åberg, D. Kult, and E. Sjöqvist, Phys. Rev. A **72**, 042317 (2005).
- [26] J. Roland and N. J. Cerf, Phys. Rev. A **71**, 032330 (2005).
- [27] T. Albash and D. A. Lidar, Phys. Rev. A **91**, 062320 (2015).
- [28] T. Yamamoto, K. Inomata, M. Watanabe, K. Matsuba, T. Miyazaki, W. D. Oliver, Y. Nakamura, and J. S. Tsai, Applied Physics Letters **93**, 042510 (2008).
- [29] W. Wustmann and V. Shumeiko, Phys. Rev. B **87**, 184501 (2013).
- [30] See supplemental material at [URL provided by publisher].
- [31] H. Goto, Scientific Reports **6**, 21686 EP (2016).
- [32] H. Goto, Phys. Rev. A **93**, 050301 (2016).
- [33] S. Puri and A. Blais, arXiv:1605.09408 (2016).
- [34] Z. Wang, A. Marandi, K. Wen, R. L. Byer, and Y. Yamamoto, Phys. Rev. A **88**, 063853 (2013).
- [35] R. Hamerly and H. Mabuchi, Phys. Rev. Applied **4**, 024016 (2015).
- [36] K. Takata, A. Marandi, and Y. Yamamoto, Phys. Rev. A **92**, 043821 (2015).
- [37] S. E. Nigg, H. Paik, B. Vlastakis, G. Kirchmair, S. Shankar, L. Frunzio, M. H. Devoret, R. J. Schoelkopf, and S. M. Girvin, Phys. Rev. Lett. **108**, 240502 (2012).
- [38] J. Bourassa, F. Beaudoin, J. M. Gambetta, and A. Blais, Phys. Rev. A **86**, 013814 (2012).
- [39] G. Kirchmair, B. Vlastakis, Z. Leghtas, S. E. Nigg, H. Paik, E. Ginossar, M. Mirrahimi, L. Frunzio, S. M. Girvin, and R. J. Schoelkopf, Nature **495**, 205 (2013), ISSN 0028-0836.
- [40] M. H. Devoret, *Quantum Fluctuations in Electrical Circuits* (Elsevier Science B. V., 1995), chap. 10, p. 351, Les Houches, Session LXIII, les Houches, Session LXIII.
- [41] D. Venturelli, S. Mandrà, S. Knysh, B. O’Gorman, R. Biswas, and V. Smelyanskiy, Phys. Rev. X **5**, 031040 (2015).
- [42] V. V. Ryazanov, V. A. Oboznov, A. Y. Rusanov, A. V. Veretenikov, A. A. Golubov, and J. Aarts, Phys. Rev. Lett. **86**, 2427 (2001).
- [43] E. C. Gingrich, B. M. Niedzielski, J. A. Glick, Y. Wang, D. L. Miller, R. Loloee, W. P. Pratt Jr, and N. O. Birge, Nat Phys **12**, 564 (2016), ISSN 1745-2473, letter.
- [44] T. Kontos, M. Aprili, J. Lesueur, F. Genêt, B. Stephanidis, and R. Boursier, Phys. Rev. Lett. **89**, 137007 (2002).
- [45] J. Park, J. Lu, S. Stemmer, and R. A. York, in *Applications of Ferroelectrics, 2004. ISAF-04. 2004 14th IEEE International Symposium on* (2004), pp. 17–20.
- [46] K. Cicak, D. Li, J. A. Strong, M. S. Allman, F. Altomare, A. J. Sirois, J. D. Whittaker, J. D. Teufel, and R. W. Simmonds, Applied Physics Letters **96**, 093502 (2010).
- [47] H. Wiseman and G. Milburn, *Quantum Measurement and Control* (Cambridge University Press, 2010), ISBN 9780521804424.
- [48] L. C. Venuti, T. Albash, D. A. Lidar, and P. Zanardi, Phys. Rev. A **93**, 032118 (2016).
- [49] J. Johansson, P. Nation, and F. Nori, Computer Physics Communications **183**, 1760 (2012).

Supplementary Material for “Robust quantum optimizer with full connectivity”

Simon E. Nigg, Niels Lörch and Rakesh P. Tiwari
(Dated: September 20, 2016)

CONTENTS

I. Derivation of the circuit Hamiltonian	1
A. AC modulated split Josephson junction as a parametric oscillator	1
1. Ac flux modulation	2
2. Expansion of the Josephson nonlinearity	3
3. Canonical quantization	3
B. Shunted chain of parametric oscillators	4
C. Minima of the potential energy with half flux quantum flux bias	4
D. Expansion of the Josephson potential of the shunt: All-to-all coupling	5
1. Canonical quantization	5
II. Readout and dissipation	6
A. Homodyne measurement via capacitively coupled transmission lines	6
III. Two coupled parametric oscillators	7
A. Instantaneous eigenspectrum in the rotating frame	7
1. Diabatic transitions	8
B. Semiclassical analysis	9
1. Steady states	9
2. Linear stability	10
C. Entanglement	11
D. Robustness to photon dephasing	12
E. Quantum trajectories comparison between CVIM and QA	13
IV. Typical quantum trajectories for the number partitioning problem	13
References	17

I. DERIVATION OF THE CIRCUIT HAMILTONIAN

We start by describing an individual split Josephson junction with ac flux bias. We then discuss the condition for achieving anti-ferromagnetic all-to-all coupling between N Kerr parametric oscillators (KPOs) connected in series and derive the Hamiltonian of the quantum Ising machine described in the main text.

A. AC modulated split Josephson junction as a parametric oscillator

Consider a small loop of superconductor interrupted twice by a normal tunnel junction forming two identical Josephson junctions. The ring is assumed to be small enough so that its inductance is dominated by the Josephson inductances. The Lagrangian is then

$$\mathcal{L}_0 = \frac{1}{2} C_J (\dot{\varphi}_1^2 + \dot{\varphi}_2^2) + E_J (\cos \varphi_1 + \cos \varphi_2). \quad (1)$$

Here, for convenience, we have chosen units such that the flux quantum $\Phi_0 = h/(2e) = 2\pi$. The parameters C_J and E_J denote the capacitance and Josephson energy of each Josephson junction. The variables φ_1 and φ_2 are not independent.

If a flux Φ is threaded through the loop, then flux quantization requires that $\varphi_1 + \varphi_2 = \Phi$. It is convenient to change variables as

$$\chi_i = \varphi_i - \frac{\Phi}{2}. \quad (2)$$

Then $\chi_1 + \chi_2 = 0$ and $\chi_1 - \chi_2 = \varphi_1 - \varphi_2 \equiv 2\theta$ and the Lagrangian becomes

$$\mathcal{L}_0 = \frac{1}{2}C\dot{\theta}^2 + 2E_J \cos(\Phi/2) \cos \theta, \quad (3)$$

with $C = 2C_J$. Here we have used that $d(\chi_1 + \chi_2)/dt = 0$ and we have neglected a time dependent term $\frac{1}{4}C_J\dot{\Phi}^2$, which is independent of the coordinates and does not affect the Euler Lagrange equations. Note that this lumped element circuit describes a parametric oscillator and is essentially equivalent to the one used to describe the Josephson parametric amplifier^{1,2}.

A tunable capacitor, required to achieve tunable couplings (see Methods in the main text), can be added in parallel with the Josephson capacitance as illustrated in Fig. 1. The total capacitance is then the sum of the tunable capacitance and the Josephson capacitances.

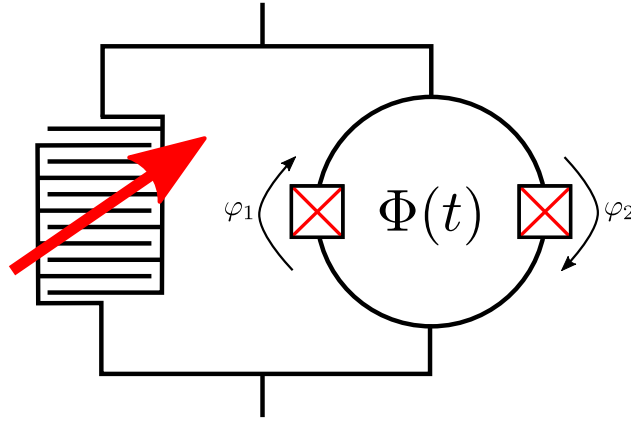


FIG. 1. Illustration of a SQUID based Kerr parametric oscillator circuit. The square boxes with red crosses represent the Josephson junctions while the interdigitated diagram on the left represents a tunable capacitor.

The Hamiltonian function is obtained as usual by introducing the momentum conjugate to the variable θ as

$$q \equiv \frac{1}{2e} \frac{\partial \mathcal{L}_0}{\partial \dot{\theta}} = \frac{C}{2e} \dot{\theta}. \quad (4)$$

Then a Legendre transformation yields

$$\mathcal{H}_0 = 2eq\dot{\theta} - \mathcal{L}_0 = 4E_C q^2 - 2E_J \cos(\Phi/2) \cos \theta, \quad (5)$$

where we have defined the single electron charging energy $E_C = e^2/(2C)$.

1. Ac flux modulation

Next, we consider a monochromatic flux modulation of the form

$$\Phi(t)/2 = \Phi^{\text{dc}} + \delta\Phi(t), \quad (6)$$

with $\delta\Phi(t) = \delta\Phi^{\text{ac}} \sin(\Omega t + \phi)$. Then we have

$$\cos(\Phi(t)/2) = \cos(\Phi^{\text{dc}}) \cos(\delta\Phi^{\text{ac}} \sin(\Omega t + \phi)) - \sin(\Phi^{\text{dc}}) \sin(\delta\Phi^{\text{ac}} \sin(\Omega t + \phi)) \quad (7)$$

$$= \cos(\Phi^{\text{dc}}) \left\{ J_0(\delta\Phi^{\text{ac}}) + 2 \sum_{m=1}^{\infty} J_{2m}(\delta\Phi^{\text{ac}}) \cos[2m(\Omega t + \phi)] \right\} \quad (8)$$

$$- 2 \sin(\Phi^{\text{dc}}) \sum_{m=0}^{\infty} J_{2m+1}(\delta\Phi^{\text{ac}}) \sin[(2m+1)(\Omega t + \phi)]. \quad (9)$$

If $|\delta\Phi^{\text{ac}}| \ll 1$, then we can keep in the sums only terms with J_0, J_1 , yielding

$$\cos(\Phi(t)/2) \simeq \cos(\Phi^{\text{dc}})J_0(\delta\Phi^{\text{ac}}) - 2\sin(\Phi^{\text{dc}})J_1(\delta\Phi^{\text{ac}})\sin(\Omega t + \phi). \quad (10)$$

It is convenient to separate the Hamiltonian into an explicitly time independent and an explicitly time dependent part as $\mathcal{H}_0 = \mathcal{H}_1 + \mathcal{H}_2(t)$, where

$$\mathcal{H}_1 = 4E_C q^2 - 2E_J \cos(\Phi^{\text{dc}})J_0(\delta\Phi^{\text{ac}})\cos\theta, \quad (11)$$

and

$$\mathcal{H}_2(t) = 4E_J \sin(\Phi^{\text{dc}})J_1(\delta\Phi^{\text{ac}})\sin(\Omega t + \phi)\cos\theta. \quad (12)$$

2. Expansion of the Josephson nonlinearity

We are ultimately interested in the transmon regime³ where $E_J \gg E_C$. In this case we can expand the $\cos\theta$ term around the local minimum of the classical potential $\theta = 0$, and keep only the leading nonlinearity. Furthermore, since we focus on the case of weak ac modulation, where $\delta\Phi^{\text{ac}} \ll \Phi_0$ (in physical units), we can neglect the nonlinear part of the time dependent term and approximate $J_0(x) \simeq 1$ and $J_1(x) \simeq x/2$. Therefore, dropping c-number terms which do not contribute to the dynamics, we have

$$\mathcal{H}_1 \simeq 4E_C q^2 + E_J \cos(\Phi^{\text{dc}})\theta^2 - \frac{E_J}{12} \cos(\Phi^{\text{dc}})\theta^4, \quad (13)$$

$$\mathcal{H}_2 \simeq -E_J \sin(\Omega t + \phi) \sin(\Phi^{\text{dc}})\delta\Phi^{\text{ac}}\theta^2. \quad (14)$$

3. Canonical quantization

The quantum model is introduced by replacing the generalized coordinates θ and q by canonically conjugate operators $\boldsymbol{\theta}$ and \mathbf{q} with commutator³ $[\boldsymbol{\theta}, \mathbf{q}] = i$. It is then convenient to work in the basis which diagonalizes the quadratic part of \mathbf{H}_1 . This is achieved by introducing the bosonic creation and annihilation operators \mathbf{a}^\dagger and \mathbf{a} , with commutator $[\mathbf{a}, \mathbf{a}^\dagger] = 1$, defined as

$$\boldsymbol{\theta} = \sqrt{\frac{Z}{2}} (\mathbf{a} + \mathbf{a}^\dagger), \quad (15)$$

$$\mathbf{q} = -i\sqrt{\frac{1}{2Z}} (\mathbf{a} - \mathbf{a}^\dagger). \quad (16)$$

Here we have defined the mode impedance

$$Z = \sqrt{\frac{4E_C}{E_J \cos(\Phi^{\text{dc}})}}. \quad (17)$$

Thus the Hamiltonian becomes

$$\mathbf{H}_1 = \omega \mathbf{a}^\dagger \mathbf{a} - \frac{E_C}{12} (\mathbf{a} + \mathbf{a}^\dagger)^4, \quad (18)$$

$$\mathbf{H}_2 = -\frac{E_J}{2} Z \sin(\Omega t + \phi) \sin(\Phi^{\text{dc}}) \delta\Phi^{\text{ac}} (\mathbf{a} + \mathbf{a}^\dagger)^2. \quad (19)$$

Here we have defined the oscillator harmonic frequency

$$\omega = 4\sqrt{E_C E_J \cos(\Phi^{\text{dc}})}. \quad (20)$$

Next, we use the rotation wave approximation (RWA) twice. The first time, to eliminate the counter-rotating terms in the quartic terms in \mathbf{H}_1 . Normal ordering yields

$$: (\mathbf{a} + \mathbf{a}^\dagger)^4 : = \mathbf{a}^{4\dagger} + 6\mathbf{a}^{2\dagger} + 4(\mathbf{a}^{3\dagger}\mathbf{a}) + 6(\mathbf{a}^{2\dagger}\mathbf{a}^2) + 4(\mathbf{a}^\dagger\mathbf{a}^3) + 12(\mathbf{a}^\dagger\mathbf{a}) + \mathbf{a}^4 + 6\mathbf{a}^2 + 3 \quad (21)$$

Hence the non-rotating terms are $6\mathbf{a}^{\dagger 2}\mathbf{a}^2$ and $12\mathbf{a}^{\dagger}\mathbf{a}$. The latter leads to a small renormalization of the oscillator frequency by an amount $\Delta\omega = -E_C$. Henceforth, we shall absorb this term in an implicit redefinition of the oscillator frequency. The second application of the RWA is with respect to the drive. Here we specifically consider a drive frequency close to twice the oscillator frequency $\Omega \simeq 2\omega$. Then if we furthermore choose the drive phase $\phi = -\pi/2$, the only resonant terms in \mathbf{H}_2 are the ones proportional to $\mathbf{a}^2 e^{i\Omega t}$ and $\mathbf{a}^{\dagger 2} e^{-i\Omega t}$. Putting it all together, we obtain the Hamiltonian of the KPO

$$\mathbf{H} = \omega \mathbf{a}^{\dagger} \mathbf{a} - \frac{E_C}{2} \mathbf{a}^{\dagger} \mathbf{a}^{\dagger} \mathbf{a} \mathbf{a} + \frac{E_J}{4} Z \sin(\Phi^{\text{dc}}) \delta\Phi^{\text{ac}} \left(\mathbf{a}^2 e^{i\Omega t} + \mathbf{a}^{\dagger 2} e^{-i\Omega t} \right). \quad (22)$$

B. Shunted chain of parametric oscillators

Next, we consider a chain of KPOs shunted by a large area Josephson junction and revert to the notation used in the main text denoting with φ_n the phase drop across oscillator $n \in \{1, \dots, N\}$. The phase drop across the shunt junction is denoted with φ_0 . The total Lagrangian of the shunted chain of KPOs depicted in Fig. 1 of the main text is

$$\mathcal{L} = E_J^{(0)} \cos(\varphi_0) + \sum_{n=1}^N \mathcal{L}_n, \quad (23)$$

where $E_J^{(0)}$ denotes the Josephson energy of the shunt and \mathcal{L}_n are the Lagrangians of the individual KPOs (3) with $\theta \rightarrow \varphi_n$. Here we have neglected the capacitive energy of the large area shunt junction, assuming that its capacitance is sufficiently large such that $E_C^{(0)}/E_J^{(0)} \approx 0$. The phase variables $\varphi_0, \varphi_1, \dots, \varphi_N$ are not independent. Flux quantization requires that

$$\varphi_0 = \Phi_e - \sum_{n=1}^N \varphi_n. \quad (24)$$

Here Φ_e denotes the flux bias through the loop formed by the chain and the shunt.

C. Minima of the potential energy with half flux quantum flux bias

When deriving the quantum Hamiltonian of the circuit, it is important to expand around a classical minimum of the potential. In terms of the N independent variables $\varphi_1, \dots, \varphi_N$, the potential energy is

$$\mathcal{U} = -E_J^{(0)} \cos\left(\Phi_e - \sum_{n=1}^N \varphi_n\right) - 2E_J \sum_{n=1}^N \cos\left(\Phi_n^{\text{dc}}\right) J_0(\delta\Phi_n^{\text{ac}}) \cos(\varphi_n). \quad (25)$$

The location of the minima depends on the flux bias Φ_e . When $\Phi_e = 0$, then the point $\varphi_1 = \varphi_2 = \dots = \varphi_N = 0$ is a local minimum. Of special interest for implementing anti-ferromagnetic coupling is the case $\Phi_e = \pi$, corresponding to half a flux quantum. In this case the potential energy is

$$\mathcal{U} = E_J^{(0)} \cos\left(\sum_{n=1}^N \varphi_n\right) - \sum_{n=1}^N E_J^{(n)} \cos(\varphi_n), \quad (26)$$

where we have defined $E_J^{(n)} = 2E_J \cos(\Phi_n^{\text{dc}}) J_0(\delta\Phi_n^{\text{ac}})$. The minima of the potential satisfy

$$\partial_{\varphi_n} \mathcal{U} = 0 \Leftrightarrow E_J^{(n)} \sin(\varphi_n) = E_J^{(0)} \sin\left(\sum_{n=1}^N \varphi_n\right). \quad (27)$$

This implies that $\varphi_n - \varphi_m = 2\pi k$ or $\varphi_n + \varphi_m = (2k+1)\pi$ with $k \in \mathbb{Z}$. Let us focus on the case where $|\varphi_n| \ll \pi$, which is shown to be consistent a posteriori. In this case we can only have the branch of solutions satisfying $\varphi_n - \varphi_m = 2\pi k$. Then

$$\varphi_n \simeq \sin(\varphi_n) = \frac{E_J^{(0)}}{E_J^{(n)}} \sin(N\varphi_n). \quad (28)$$

If now we further require that $NE_J^{(0)} < E_J^{(n)}$, then only one solution of the transcendental equation (28) exists namely $\varphi_n = 0$. Physically, this condition means that the potential of the shunt junction is much softer than the potential of the chain junctions. Therefore, in the ground state it is preferable to minimize the energy stored in the stiff chain junctions while allowing a larger deviation of φ_0 across the soft shunt junction away from its equilibrium value π .

D. Expansion of the Josephson potential of the shunt: All-to-all coupling

Having established the condition for a local minimum of the potential at $\varphi_1 = \varphi_2 = \dots = \varphi_N = 0$ when $\Phi_e = \pi$, we next expand the potential energy around this point up to the leading non-linearity. This procedure is very similar to the one discussed in I A 2 and we only point out the differences here. With the flux bias $\Phi_e = \pi$, the shunt contributes a term to the Hamiltonian

$$\mathcal{H}_S = E_J^{(0)} \cos\left(\sum_{n=1}^N \varphi_n\right). \quad (29)$$

Since $NE_J^{(0)} < E_J$, we neglect the nonlinear contribution and expanding the cosine to leading order. Suppressing an unimportant c-number term we then have

$$\mathcal{H}_S \simeq -\frac{E_J^{(0)}}{2} \sum_{n=1}^N \varphi_n^2 - \frac{E_J^{(0)}}{2} \sum_{n \neq m} \varphi_n \varphi_m. \quad (30)$$

The full Hamiltonian is thus (see Eqs. (13) and (14))

$$\mathcal{H} = 4 \sum_{n=1}^N E_C^{(n)} q_n^2 - \sum_{n=1}^N \left[E_J^{(n)} \cos(\Phi_n^{\text{dc}}) - \frac{E_J^{(0)}}{2} \right] \varphi_n^2 - \sum_{n=1}^N \frac{E_J^{(n)}}{12} \cos(\Phi_n^{\text{dc}}) \varphi_n^4 - \sum_{n=1}^N \sin(\Omega_n t + \phi_n) \sin(\Phi_n^{\text{dc}}) \delta \Phi_n^{\text{ac}} \varphi_n^2 - \frac{E_J^{(0)}}{2} \sum_{n \neq m} \varphi_n \varphi_m. \quad (31)$$

1. Canonical quantization

Quantization is similar to the case of single parametric oscillator in Section. I A 3. The only difference is that the mode impedances and frequencies also depend on $E_J^{(0)}$ as follows

$$\omega_n = 4 \sqrt{E_C^{(n)} \left[E_J^{(n)} \cos(\Phi_n^{\text{dc}}) - \frac{E_J^{(0)}}{2} \right]}, \quad (32)$$

$$Z_n = \sqrt{\frac{4E_C^{(n)}}{E_J^{(n)} \cos(\Phi_n^{\text{dc}}) - \frac{E_J^{(0)}}{2}}} = \frac{8E_C^{(n)}}{\omega_n}. \quad (33)$$

Finally, choosing the drive frequencies $\Omega_n \approx 2\omega_n$, setting $\phi_n = -\pi/2$ and applying the RWA, the Hamiltonian of N coupled KPOs with all-to-all anti-ferromagnetic coupling is

$$\mathbf{H} = \sum_{n=1}^N \omega_n \mathbf{a}_n^\dagger \mathbf{a}_n + \sum_{n=1}^N \varepsilon_n \left(e^{i\Omega_n t} \mathbf{a}_n^2 + e^{-i\Omega_n t} \mathbf{a}_n^{\dagger 2} \right) + \sum_{n \neq m} J_{nm} \mathbf{a}_n^\dagger \mathbf{a}_m - \sum_{n=1}^N K_n \mathbf{a}_n^\dagger \mathbf{a}_n^\dagger \mathbf{a}_n \mathbf{a}_n, \quad (34)$$

with

$$\varepsilon_n \simeq \frac{E_J^{(n)}}{4} Z_n \sin(\Phi_n^{\text{dc}}) \delta \Phi_n^{\text{ac}}, \quad (35)$$

$$J_{nm} \simeq -\frac{E_J^{(0)}}{2} \sqrt{Z_n Z_m}, \quad (36)$$

$$K_n \simeq \frac{E_C^{(n)}}{2}. \quad (37)$$

II. READOUT AND DISSIPATION

To read out the phase of each KPO at the end of the annealing procedure, one can capacitively couple each oscillator to a transmission line as shown in Fig. 1 of the main text. The phase shift of photons reflected back from the system can then be measured using a standard homodyne detection scheme.

A. Homodyne measurement via capacitively coupled transmission lines

In RWA, the full Hamiltonian of the system, including the quantized modes $b_n(\omega)$ of the semi-infinite transmission lines, is then $H_{\text{SB}} = H + H_{\text{TL}}$ with H given in Eq. (34) and

$$H_{\text{TL}} = \sum_{n=1}^N \int_0^\infty d\omega \sqrt{\frac{\kappa_n(\omega)}{2\pi}} \left[b_n^\dagger(\omega) a_n + a_n^\dagger b_n(\omega) \right] + \sum_n \int_0^\infty d\omega \omega b_n^\dagger(\omega) b_n(\omega). \quad (38)$$

From this model, we can derive in the usual white noise approximation $\kappa_n(\omega) = \kappa_n$, the quantum Langevin equation of motion for the oscillator modes. They read

$$\dot{a}_n(t) = -i[a_n(t), H(t)] + \frac{\kappa_n}{2} a_n(t) - \sqrt{\kappa_n} b_n^{(\text{out})}(t). \quad (39)$$

Here the output field is defined as

$$b_n^{(\text{out})}(t) = \frac{i}{\sqrt{2\pi}} \int_{-\infty}^\infty d\omega e^{-i\omega(t-t_1)} b_n(\omega, t_1), \quad (40)$$

with $t_1 > t$. Performing the above commutator we find

$$\dot{a}_n(t) = -i\omega_n a_n(t) - i \sum_{m \neq n} J_{nm} a_m(t) + 2iK_n a_n^\dagger a_n - 2i\varepsilon_n e^{-i\Omega_n t} a_n^\dagger(t) - \frac{\kappa_n}{2} a_n(t) + \sqrt{\kappa_n} b_n^{(\text{in})}(t). \quad (41)$$

Furthermore, the standard input-output relation holds

$$b_n^{(\text{in})}(t) + b_n^{(\text{out})}(t) = \sqrt{\kappa_n} a_n(t). \quad (42)$$

Clearly an exact solution of Eqs. (41) and (42) is complicated by the presence of the Kerr nonlinearity and the long-range coupling. For any finite number of oscillators N , the solution below threshold can be obtained by inversion of a linear system of equations⁴. Of particular interest here is the regime far above threshold, where we can use the semi-classical approximation and replace a_n with $\alpha_n = \pm |\alpha_n| e^{i\phi_n}$, the steady state amplitude of oscillator n . In contrast to the readout of a qubit dispersively coupled to a resonator, we do not need to drive the transmission line since the oscillators are pumped via the ac flux modulation. At zero temperature, the input is thus the vacuum noise $b_0^{(\text{in})}$. The output is then

$$b_n^{(\text{out})} = \pm \sqrt{\kappa_n} |\alpha_n| e^{i\phi_n} - b_0^{(\text{in})}. \quad (43)$$

By mixing this signal, at a beam splitter, with a strong coherent local oscillator with fixed reference phase and carrying a photon flux $\sqrt{\kappa_n} \gamma_n^{(\text{LO})}$ we have

$$b_n^{(\text{out})} = \sqrt{\kappa_n} \left(\pm r |\alpha_n| e^{i\phi_n} + t \gamma_n^{(\text{LO})} \right) - r b_0^{(\text{in})}, \quad (44)$$

where r and t denote the reflection and transmission amplitudes of the beam splitter. Thus we can detect the phase of the oscillator amplitude in the modulation of the output photon number

$$\int_0^T dt \langle b_n^{(\text{out})\dagger} b_n^{(\text{out})} \rangle = N_n^{(0)} \pm r t \kappa_n T \left(|\alpha_n| e^{-i\phi_n} \gamma_n^{(\text{LO})} + |\alpha_n| e^{i\phi_n} \gamma_n^{(\text{LO})*} \right). \quad (45)$$

Here $N_n^{(0)} = (|r \gamma_n^{(\text{LO})}|^2 + |t \alpha_n|^2) T \simeq |r \gamma_n^{(\text{LO})}|^2 T$, for $r \gg t$. Maximal contrast is obtained by tuning the phase of the local oscillator to ϕ_n . Then

$$\Delta N_n^{\text{out}} = \pm r t \kappa_n T |\alpha_n \gamma_n^{(\text{LO})}|. \quad (46)$$

The coupling via the transmission lines opens up a decoherence channel via photon loss. In the main text we use a master equation (Eq. (11)) to describe such losses, which is equivalent to the quantum Langevin equation (41) with a zero temperature bath.

III. TWO COUPLED PARAMETRIC OSCILLATORS

In the main text, we provide an intuitive picture in terms of the symmetric and anti-symmetric modes. Here we provide a complementary discussion of the dynamics of two coupled KPOs in the original basis. We consider two driven symmetric coupled KPOs. This system is described by the Hamiltonian

$$H_2 = \omega(a^\dagger a + b^\dagger b) + \varepsilon(a^2 e^{i\Omega t} + a^{\dagger 2} e^{-i\Omega t}) - K(a^\dagger a^\dagger a a + b^\dagger b^\dagger b b) + J(a^\dagger b + b^\dagger a). \quad (47)$$

Here we are interested in the case where $\Omega = 2(\omega - \Delta)$ with $|\Delta| \ll |\omega|$. Transforming to a frame rotating with the frequency $\Omega/2$, via the unitary transformation $\exp[i(\Omega/2)t(a^\dagger a + b^\dagger b)]$, we have

$$\tilde{H}_2 = -K\left(a^{\dagger 2} - \frac{\varepsilon}{K}\right)\left(a^2 - \frac{\varepsilon}{K}\right) - K\left(b^{\dagger 2} - \frac{\varepsilon}{K}\right)\left(b^2 - \frac{\varepsilon}{K}\right) + J(a^\dagger b + b^\dagger a) + \Delta(a^\dagger a + b^\dagger b) + \frac{2\varepsilon^2}{K}. \quad (48)$$

A. Instantaneous eigenspectrum in the rotating frame

We begin by describing the low photon number part of the spectrum of (48). At zero drive strength $\varepsilon = 0$, the total number of photons shared by the two oscillators is conserved and the sector with up to one photon can be immediately diagonalized. The three states $|0, 0\rangle$, $\frac{1}{\sqrt{2}}(|0, 1\rangle + |1, 0\rangle)$ and $\frac{1}{\sqrt{2}}(|0, 1\rangle - |1, 0\rangle)$, are eigenstates with corresponding eigenvalues $E_0 = 0$, $E_+ = \Delta + J$ and $E_- = \Delta - J$. Note that the corresponding energies in the “lab” frame (ignoring the zero point energy) are $E_0^{\text{lab}} = 0$, $E_\pm^{\text{lab}} = \omega \pm J$. Hence we see that if $\Delta \pm J < 0 \Leftrightarrow \Omega > 2(\omega \pm J)$, then the vacuum is guaranteed to be the state with the highest energy. The fact that the Hamiltonian (48) is not bounded from below need not alarm us if we keep in mind how it was derived by truncating the expansion of the Josephson potential and if we also keep in mind that photon losses, once included, will naturally tend to move the state towards lower photon numbers. This means however that we must now think of the instantaneous “ground state” in the rotating frame, where the Hamiltonian is time independent, as the state with highest energy instead of the more usual lowest energy state in a stationary system. For lack of a better word, we shall call this state the roof state.

The two-photon sector is spanned by the three states $|2, 0\rangle$, $|1, 1\rangle$ and $|0, 2\rangle$. In this basis the two-photon block of the Hamiltonian at zero drive is in the rotating frame

$$H_2^{(2)} = \begin{pmatrix} 2(\Delta - K) & J & 0 \\ J & 2\Delta & J \\ 0 & J & 2(\Delta - K) \end{pmatrix}. \quad (49)$$

The three eigenstates and corresponding eigenvalues are:

Eigenvector	Eigenvalue	Energy in “lab” frame
$\frac{1}{\sqrt{2}}(2, 0\rangle - 0, 2\rangle)$	$2(\Delta - K)$	$2(\omega - K)$
$\frac{ J }{\sqrt{2(K^2+2J^2)}} \sqrt{1 - \frac{K}{\sqrt{K^2+2J^2}}} (2, 0\rangle + 0, 2\rangle) + \text{sign}(J) \frac{1}{\sqrt{2}} \sqrt{1 - \frac{K}{\sqrt{K^2+2J^2}}} 1, 1\rangle$	$2\Delta - K - \sqrt{K^2 + 2J^2}$	$2\omega - K - \sqrt{K^2 + 2J^2}$
$\frac{ J }{\sqrt{2(K^2+2J^2)}} \sqrt{1 + \frac{K}{\sqrt{K^2+2J^2}}} (2, 0\rangle + 0, 2\rangle) - \text{sign}(J) \frac{1}{\sqrt{2}} \sqrt{1 + \frac{K}{\sqrt{K^2+2J^2}}} 1, 1\rangle$	$2\Delta - K + \sqrt{K^2 + 2J^2}$	$2\omega - K + \sqrt{K^2 + 2J^2}$

As long as the Kerr-nonlinearity and the coupling are sufficiently weak such that $\omega \pm J > 2K$ and $\omega - K - \sqrt{K^2 + 2J^2}$, then the single-photon states have higher energy than the two-photon states.

In the opposite limit of large two-photon drive strength, $\varepsilon \gg \sqrt{\frac{K}{2}}|\Delta \pm J|$, we can treat the terms $\sim J, \Delta$ perturbatively. To leading order, the eigenstates and eigenenergies are given by the two mode cat states listed in the following table:

Eigenvector	Eigenvalue
$ \psi_+\rangle = \frac{1}{N_+}(\alpha, \alpha\rangle + -\alpha, -\alpha\rangle)$	$\frac{N_+^2}{N_-^2}(\Delta + J) \alpha ^2 = \tanh\left(\frac{2\varepsilon}{K}\right)(\Delta + J)\frac{\varepsilon}{K}$
$ \psi_-\rangle = \frac{1}{N_-}(\alpha, \alpha\rangle - -\alpha, -\alpha\rangle)$	$\frac{N_+^2}{N_-^2}(\Delta + J) \alpha ^2 = \coth\left(\frac{2\varepsilon}{K}\right)(\Delta + J)\frac{\varepsilon}{K}$
$ \phi_+\rangle = \frac{1}{N_+}(\alpha, -\alpha\rangle + -\alpha, \alpha\rangle)$	$\frac{N_+^2}{N_-^2}(\Delta - J) \alpha ^2 = \tanh\left(\frac{2\varepsilon}{K}\right)(\Delta - J)\frac{\varepsilon}{K}$
$ \phi_-\rangle = \frac{1}{N_-}(\alpha, -\alpha\rangle - -\alpha, \alpha\rangle)$	$\frac{N_+^2}{N_-^2}(\Delta - J) \alpha ^2 = \coth\left(\frac{2\varepsilon}{K}\right)(\Delta - J)\frac{\varepsilon}{K}$

Here the amplitude is $\alpha \simeq \sqrt{\varepsilon/K}$ and the cat-state normalization factors are $\mathcal{N}_{\pm} = \sqrt{2} \sqrt{1 \pm e^{-4|\alpha|^2}}$. Note that the states $|\phi_{+}\rangle$ and $|\psi_{+}\rangle$ have even total photon number parity, i.e. they are eigenstates of the parity operator $\Pi_2 = \exp[-i\pi(a^{\dagger}a + b^{\dagger}b)]$, with eigenvalue +1. The states $|\psi_{-}\rangle$ and $|\phi_{-}\rangle$ have odd parity.

For $J > 0$ ($J < 0$), the state $|\psi_{+}\rangle$ ($|\phi_{+}\rangle$) is the highest energy state (i.e. the roof state). Furthermore, since two-photon drive conserves the total photon number parity, it is clear that the vacuum state at $\varepsilon = 0$ is adiabatically connected with an even photon number parity state at large ε : For $J > 0$ with $|\psi_{+}\rangle$ and for $J < 0$ with $|\phi_{+}\rangle$. Similarly, the two excited states with one photon when $\varepsilon = 0$ are adiabatically connected with the odd photon number parity states $|\psi_{-}\rangle$ and $|\phi_{-}\rangle$. Schematically:

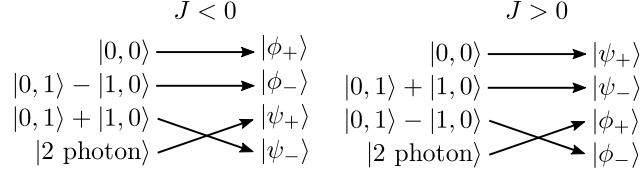


Fig. 2 shows the numerically computed highest part of the instantaneous eigenspectrum of (49). The parameter values used are given in the caption. Note that for $\varepsilon > 0$, this spectrum does not reflect the energy of the system. Indeed, for $\varepsilon \neq 0$, the system is driven and there are no stationary energy eigenstates. Nevertheless, this figure is useful because the adiabatic evolution proceeds along the curves in this spectrum. Interestingly, we find generically, that there are points of crossing (diaboli points⁵), between excited states of different total photon number parity at certain values of the two-photon drive strength.

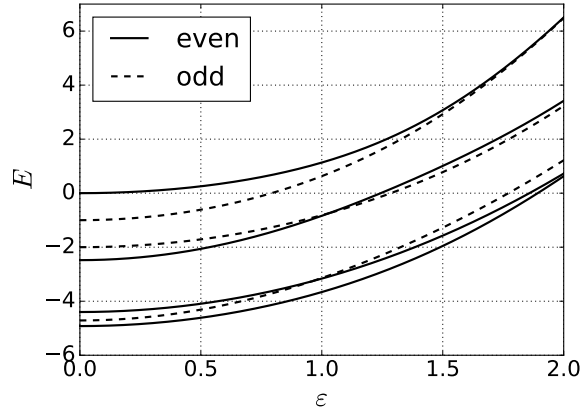


FIG. 2. Highest part of the eigenspectrum of two coupled parametric oscillators in the rotating frame. Solid lines correspond to states with even total photon number parity, while odd lines correspond to states with odd total photon number parity. Notice the crossing points in the spectrum between lines corresponding to excited states with different total photon number parity. These are examples of so-called diaboli points⁵. The parameters used are: $\Delta/\hbar = -1.5$ MHz, $K/\hbar = 0.7$, $T \in (0.1, 400)\mu\text{s}$ and $\varepsilon_{\text{MAX}}/\hbar = 2$ MHz.

1. Diabatic transitions

In order to transfer the population from the vacuum at $\varepsilon = 0$ to the ground state at $\varepsilon \gg \sqrt{\frac{K}{2}}|\Delta \pm J|$, the drive strength must be increased sufficiently slowly such as to guarantee the adiabatic condition. Here we present numerical results on the breakdown of adiabaticity for two anti-ferromagnetically coupled KPOs. We focus on the case of anti-ferromagnetic coupling $J < 0$. Fig. 3 shows, with the same parameters as Fig. 2, the populations of the highest seven energy instantaneous eigenstates at the end of the ramp, i.e. at $\varepsilon(T) = \varepsilon_{\text{MAX}}$. The populations are shown as a function of increasing normalized linear ramp rate $1/T$, for a system initially in the highest energy state. Clearly, above a certain ramp rate, diabatic transitions from the ground state to other states *with the same total photon number parity*

take place. This can be inferred by comparing Fig. 3 with the spectrum values in Fig. 2 at $\varepsilon = \varepsilon_{\text{MAX}}$. This selection rule reflects the conservation of total photon number parity.

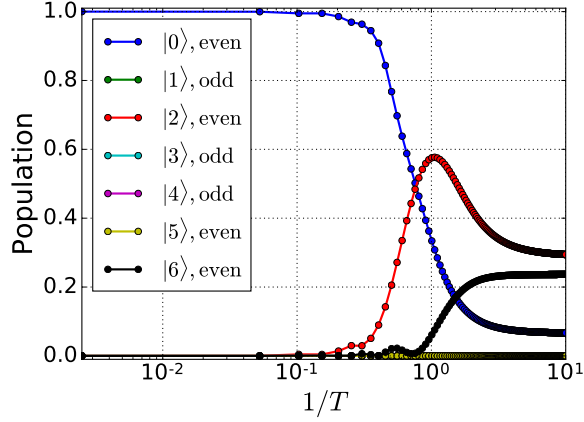


FIG. 3. Populations of the seven highest eigenstates as a function of the normalized ramp rate. The states are labeled as $|n\rangle$, with $n = 0$ denoting the highest eigenvalue. Comparing with Fig. 2, we see that population is transferred out of the highest state into states with the same even total photon number parity. The parameters used in the simulation are: $\Delta/\hbar = -1.5$ MHz, $K/\hbar = 0.7$, $T \in (0.1, 400)\mu\text{s}$ and $\varepsilon_{\text{MAX}}/\hbar = 2$ MHz.

Moving beyond the coherent limit, we next discuss the dissipative case semi-classically. One difference that is apparent from the above discussion, is that single photon loss breaks photon number parity conservation. Hence dissipative transitions between states with different total photon number parity become possible.

B. Semiclassical analysis

Here we present the key elements of the semi-classical analysis used in the manuscript to convey the intuition about the dissipative optimization process in the quantum Ising machine.

Our starting point are the semi-classical mean-field equations for two coupled oscillators, in a frame rotating with half the drive frequency $\Omega/2$. Formally they can be obtained by replacing the operators in the Heisenberg-Langevin equation with complex functions as $\mathbf{a} \rightarrow \alpha(t)$ and $\mathbf{b} \rightarrow \beta(t)$ and averaging out the noise terms. They are (see Methods in the main text)

$$i\dot{\alpha} = (\Delta - 2K|\alpha|^2)\alpha + J\beta + 2\varepsilon\alpha^* - i\frac{\kappa}{2}\alpha, \quad (50)$$

$$i\dot{\beta} = (\Delta - 2K|\beta|^2)\beta + J\alpha + 2\varepsilon\beta^* - i\frac{\kappa}{2}\beta. \quad (51)$$

1. Steady states

In the steady state we have

$$(\Delta - 2K|\alpha|^2)\alpha + J\beta + 2\varepsilon\alpha^* - i\frac{\kappa}{2}\alpha = 0, \quad (52)$$

$$(\Delta - 2K|\beta|^2)\beta + J\alpha + 2\varepsilon\beta^* - i\frac{\kappa}{2}\beta = 0. \quad (53)$$

The three solutions of interest are (i): $\alpha = \beta = 0$, which corresponds to the vacuum state, (ii): $\alpha = \beta = \alpha_s^{(\text{ii})}$, which corresponds to symmetric mode where both oscillators oscillate in phase and (iii): $\alpha = -\beta = \alpha_s^{(\text{iii})}$, which corresponds to the anti-symmetric mode where both oscillators oscillate out-of-phase by π . As explained in III A, we require that

$\Delta \pm J < 0$, such that the vacuum is the roof state. This implies that solution (ii) exists only if $\varepsilon > \frac{1}{2} \sqrt{(\Delta + J)^2 + \left(\frac{\kappa}{2}\right)^2}$, and the amplitude is then

$$\alpha_s^{(ii)} = \pm e^{i\phi} \sqrt{\frac{\sqrt{4\varepsilon^2 - \left(\frac{\kappa}{2}\right)^2} + \Delta + J}{2K}}. \quad (54)$$

Similarly, solution (iii) exists if $\varepsilon > \frac{1}{2} \sqrt{(\Delta - J)^2 + \left(\frac{\kappa}{2}\right)^2}$, and the amplitude is then

$$\alpha_s^{(iii)} = \pm e^{i\phi} \sqrt{\frac{\sqrt{4\varepsilon^2 - \left(\frac{\kappa}{2}\right)^2} + \Delta - J}{2K}}. \quad (55)$$

Here $\phi = -\frac{1}{2} \arctan \left[\frac{\kappa}{\sqrt{16\varepsilon^2 - \kappa^2}} \right]$.

2. Linear stability

Next, we analyze the linear stability of the above solutions. To this end, we substitute $\alpha(t) = \alpha_s + \Delta\alpha(t)$ and $\beta(t) = \beta_s + \Delta\beta(t)$ into (68) and linearize in $\Delta\alpha$ and $\Delta\beta$ to obtain in matrix notation

$$\frac{d}{dt} \begin{pmatrix} \Delta\alpha \\ \Delta\alpha^* \\ \Delta\beta \\ \Delta\beta^* \end{pmatrix} = \begin{pmatrix} -i\Delta + 4iK|\alpha_s|^2 - \frac{\kappa}{2} & 2i(K\alpha_s^2 - \varepsilon) & -iJ & 0 \\ -2i(K\alpha_s^{*2} - \varepsilon) & i\Delta - 4iK|\alpha_s|^2 - \frac{\kappa}{2} & 0 & iJ \\ -iJ & 0 & -i\Delta + 4iK|\beta_s|^2 - \frac{\kappa}{2} & 2i(K\beta_s^2 - \varepsilon) \\ 0 & iJ & -2i(K\beta_s^{*2} - \varepsilon) & i\Delta - 4iK|\beta_s|^2 - \frac{\kappa}{2} \end{pmatrix} \begin{pmatrix} \Delta\alpha \\ \Delta\alpha^* \\ \Delta\beta \\ \Delta\beta^* \end{pmatrix}. \quad (56)$$

We start with the solution (i), $\alpha_s = \beta_s = 0$. In this case the stability equation is

$$\frac{d}{dt} \begin{pmatrix} \Delta\alpha \\ \Delta\alpha^* \\ \Delta\beta \\ \Delta\beta^* \end{pmatrix} = \begin{pmatrix} -i\Delta - \frac{\kappa}{2} & -2i\varepsilon & -iJ & 0 \\ 2i\varepsilon & i\Delta - \frac{\kappa}{2} & 0 & iJ \\ -iJ & 0 & -i\Delta - \frac{\kappa}{2} & -2i\varepsilon \\ 0 & iJ & 2i\varepsilon & i\Delta - \frac{\kappa}{2} \end{pmatrix} \begin{pmatrix} \Delta\alpha \\ \Delta\alpha^* \\ \Delta\beta \\ \Delta\beta^* \end{pmatrix}. \quad (57)$$

The eigenvalues are

$$\lambda_{0,\pm}^{(i)} = -\frac{\kappa}{2} \pm \sqrt{4\varepsilon^2 - (\Delta + J)^2}, \quad (58)$$

$$\lambda_{1,\pm}^{(i)} = -\frac{\kappa}{2} \pm \sqrt{4\varepsilon^2 - (\Delta - J)^2}. \quad (59)$$

The stability of this solution requires that $\text{Re}[\lambda_{0,\pm}], \text{Re}[\lambda_{1,\pm}] < 0$, which in turn requires that

$$\varepsilon < \frac{1}{2} \sqrt{(\Delta \pm J)^2 + \left(\frac{\kappa}{2}\right)^2}. \quad (60)$$

Next we consider solution (ii), $\alpha_s = \beta_s = \alpha_s^{(ii)}$. The Hermitian transformation matrix (56) in this case has the same structure as the one in (57) with the replacements

$$\varepsilon \rightarrow \varepsilon - K\alpha_s^2, \quad (61)$$

$$\Delta \rightarrow \Delta - 4K|\alpha_s|^2. \quad (62)$$

Hence we can immediately write down the eigenvalues

$$\lambda_{0,\pm}^{(ii)} = -\frac{\kappa}{2} \pm \sqrt{4|\varepsilon - K\alpha_s^2|^2 - (\Delta - 4K|\alpha_s|^2 + J)^2}, \quad (63)$$

$$\lambda_{1,\pm}^{(ii)} = -\frac{\kappa}{2} \pm \sqrt{4|\varepsilon - K\alpha_s^2|^2 - (\Delta - 4K|\alpha_s|^2 - J)^2}. \quad (64)$$

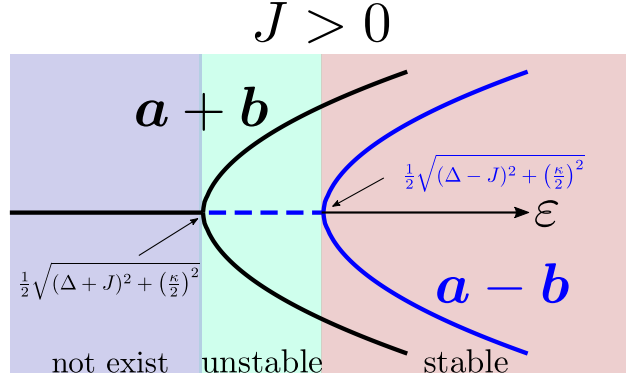


FIG. 4. Stability diagram for the symmetric mode when $J > 0$. Note that we consider the case $\Delta \pm J < 0$ throughout.

After some algebra the condition that the real parts of these eigenvalues are smaller than zero leads to the inequality

$$X + (\Delta \pm J) \sqrt{X} > 0, \quad (65)$$

with $X = 4\varepsilon^2 - \left(\frac{\kappa}{2}\right)^2$. This in turn implies that the solution is stable if and only if

$$\varepsilon > \frac{1}{2} \sqrt{(\Delta \pm J)^2 + \left(\frac{\kappa}{2}\right)^2}. \quad (66)$$

It is easy to see that solution (iii) must satisfy the same stability criterion (66) since the amplitudes only appear squared in the transformation matrix (56). Fig. 4 summarizes these results for the bifurcation behavior of the symmetric mode when $J > 0$. The situation with $J < 0$ is similar but with the roles of symmetric and anti-symmetric modes exchanged.

C. Entanglement

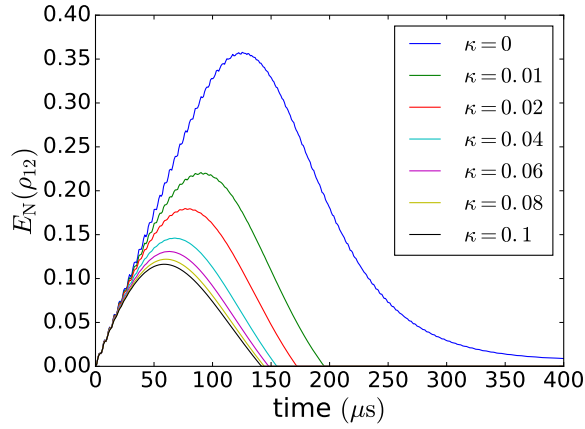


FIG. 5. Logarithmic negativity of the two-mode Gaussian state during the annealing. The covariance matrices are obtained by numerically solving the master equation (Eq. (4) of the main text). A linear ramp is used $\varepsilon(t) = \varepsilon_{\text{MAX}}(t/T)$. The parameters are: $\Delta/\hbar = -1.0$ MHz, $K/\hbar = 0.7$ MHz, $\varepsilon_{\text{MAX}}/\hbar = 2.0$ MHz and $T = 400 \mu\text{s}$.

We numerically characterize the presence of entanglement during the annealing by computing the logarithmic negativity

$$E_N(\rho_{12}) = \max(0, -\log_2(2\nu_s)), \quad (67)$$

where ν_s is the smallest symplectic eigenvalues of the partially transposed Wigner covariance matrix V of the two-mode Gaussian state⁶: $V_{ij} = (R_{ij} + R_{ji})/2$ where $R_{ij} = \langle R_i R_j \rangle - \langle R_i \rangle \langle R_j \rangle$ and $R = (\mathbf{q}_1, \mathbf{p}_1, \mathbf{q}_2, \mathbf{p}_2)$ where $\mathbf{q}_i = (\mathbf{a}_i + \mathbf{a}_i^\dagger)/\sqrt{2}$ and $\mathbf{p}_i = -i(\mathbf{a}_i - \mathbf{a}_i^\dagger)/\sqrt{2}$. The logarithmic negativity is an entanglement monotone. If $E_N = 0$ the state is separable. $E_N > 0$ indicates the presence of bipartite entanglement. Fig. 5 shows the logarithmic negativity of the state of the two coupled oscillators during the annealing for different values of the dissipation rate when starting in the two-mode vacuum. Interestingly we find that while dissipation tends to suppress entanglement, transient entanglement is present even with a finite dissipation rate.

D. Robustness to photon dephasing

In the main text we show that the continuous variable Ising machine (CVIM) displays robustness to photon loss. Here we show that it also provides protection against photon dephasing. Photon dephasing is typically not the dominant decoherence channel^{7,8}, but can arise for example as a consequence of cross-Kerr terms coupling different oscillators, which have been neglected in I D. Photon dephasing adds additional terms to the Lindblad term in the master equation, which now reads

$$\dot{\rho} = -i[\mathbf{H}, \rho] + \kappa \sum_{n=1}^N \mathcal{D}[\mathbf{a}_n] \rho + \kappa_\phi \sum_{n=1}^N \mathcal{D}[\mathbf{a}_n^\dagger \mathbf{a}_n] \rho. \quad (68)$$

Here \mathbf{H} is given by (34) in the rotating frame of the drive. In the following we generalize the arguments of Refs.^{9,10}. The master equation (68) can be written equivalently as

$$\dot{\rho} = -i(\mathbf{H}_{\text{NH}} \rho - \rho \mathbf{H}_{\text{NH}}^\dagger) + \kappa \sum_{n=1}^N \mathbf{a}_n \rho \mathbf{a}_n^\dagger + \kappa_\phi \sum_{n=1}^N \mathbf{a}_n^\dagger \mathbf{a}_n \rho \mathbf{a}_n^\dagger \mathbf{a}_n, \quad (69)$$

with the non-hermitian Hamiltonian

$$\mathbf{H}_{\text{NH}} = \mathbf{H} - i\frac{\kappa}{2} \sum_{n=1}^N \mathbf{a}_n^\dagger \mathbf{a}_n - i\frac{\kappa_\phi}{2} \sum_n \mathbf{a}_n^\dagger \mathbf{a}_n \mathbf{a}_n^\dagger \mathbf{a}_n \quad (70)$$

$$= \mathbf{H} - i\frac{\kappa + \kappa_\phi}{2} \sum_{n=1}^N \mathbf{a}_n^\dagger \mathbf{a}_n - i\frac{\kappa_\phi}{2} \sum_n \mathbf{a}_n^\dagger \mathbf{a}_n^\dagger \mathbf{a}_n \mathbf{a}_n \quad (71)$$

Hence, we see that photon dephasing results in a renormalization of the single photon loss rate: $\kappa \rightarrow \kappa + \kappa_\phi$ and in an imaginary shift of the self-Kerr term: $K \rightarrow K - i\frac{\kappa_\phi}{2}$. This will only modify the steady state value of the amplitudes but not the form of the steady state which is still a multi-mode cat state. In addition, the jump part induces random and independent rotations of the *amplitudes*. The transition rate from a configuration $\{s_1, s_2, \dots, s_n, \dots, s_N\}$ to a configuration $\{s_1, s_2, \dots, -s_n, \dots, s_N\}$ is determined by the transition rate from a coherent state $|\alpha\rangle$ to the state $|\alpha\rangle$. The latter is estimated as follows. After a jump event the state is

$$\frac{\mathbf{n}|\alpha\rangle}{\sqrt{\langle \alpha | \mathbf{n}^2 | \alpha \rangle}} = \frac{\mathbf{n}|\alpha\rangle}{\sqrt{\bar{n}(\bar{n} + 1)}} \simeq \frac{\mathbf{n}|\alpha\rangle}{\bar{n}}. \quad (72)$$

Here $\bar{n} = |\alpha|^2$ and in the last step we have assumed $\bar{n} \gg 1$. In this limit, the probability that this state is $|\alpha\rangle$ is

$$P_{|\alpha\rangle} = \frac{1}{\bar{n}^2} |\langle \alpha | \mathbf{n} | \alpha \rangle|^2 = e^{-4|\alpha|^2}. \quad (73)$$

Furthermore, the probability that in a small time interval Δt a jump happens is

$$P_{\text{jump}} = \kappa_\phi \Delta t \langle \alpha | \mathbf{n}^2 | \alpha \rangle \simeq \kappa_\phi \Delta t \bar{n}^2. \quad (74)$$

Therefore, the rate at which transitions between $|\alpha\rangle$ and $|\alpha\rangle$ occur due to dephasing is

$$\Gamma_\phi = \frac{P_{\text{jump}} P_{|\alpha\rangle}}{\Delta t} = \kappa_\phi \bar{n}^2 e^{-4|\alpha|^2}. \quad (75)$$

Hence at large amplitudes (i.e. far above threshold), the adverse effect of photon dephasing on quantum optimization with coupled KPOs is exponentially suppressed in the mean photon number of the coherent states encoding the Ising spins.

E. Quantum trajectories comparison between CVIM and QA

In Fig. 2 (b), of the main text we show a typical quantum trajectory of the quantum Ising machine with two oscillators in the adiabatic limit and in the presence of photon loss with rate $\kappa = 0.01$. Fig. 6 shows the corresponding behavior for a discrete spin-based quantum annealer with two anti-ferromagnetically coupled qubits. We use a linear ramp of the form $\varepsilon(t) = \varepsilon_{\text{MAX}}(1 - t/T)$, controlling the transverse field part of the quantum Ising model (see Eq. (1) of the main text). The left panel of Fig. 6 shows the coherent case for reference. Here we see that the optimization succeeds and the system evolves from the ground state of the transverse fields $|X_{-}\rangle|X_{-}\rangle = \frac{1}{2}(|\uparrow\rangle - |\downarrow\rangle) \otimes (|\uparrow\rangle - |\downarrow\rangle)$, to the ground state of the anti-ferromagnetic Ising model $|\phi_{+}\rangle = (|\uparrow, \downarrow\rangle + |\downarrow, \uparrow\rangle)/\sqrt{2}$. The additional states shown are $|\psi_{\pm}\rangle = (|\uparrow, \uparrow\rangle \pm |\downarrow, \downarrow\rangle)$ and $|\phi_{-}\rangle = (|\uparrow, \downarrow\rangle - |\downarrow, \uparrow\rangle)$. Note that we use the same notation as for the corresponding states of the CVIM in order to emphasize the analogy. The nature of these two sets of states is however different. While the states of the qubit based quantum annealer are eigenstates of an operator with discrete spectrum, living in a finite Hilbert space, the corresponding states of the quantum Ising machine are eigenstates of an operator with a continuous spectrum and the associated Hilbert space is infinite dimensional. The right panel of Fig. 6 shows a typical quantum trajectory for the same parameters, when the system is subject to dephasing errors with rate $\gamma/\hbar = 0.01$ MHz, in the basis that diagonalizes the Ising term, i.e. the jump operators are σ_1^z and σ_2^z . Clearly, we see that dephasing errors quickly lead to large fluctuations in the populations of the states with correct Ising encoding ($|\phi_{\pm}\rangle$). In the example shown, the state at the end of the adiabatic ramp is clearly not the ground state of the anti-ferromagnetic Ising model.

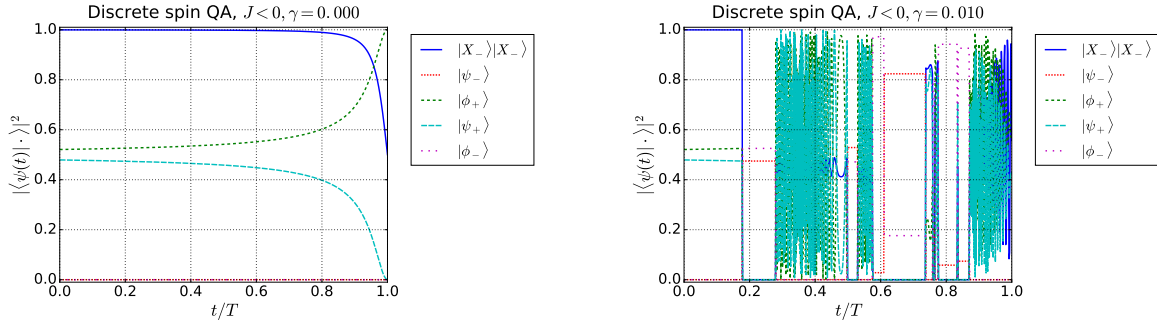


FIG. 6. Effect of dephasing on the discrete qubit quantum annealer. **Left panel:** coherent limit $\gamma = 0$. Here the annealing succeeds and the state at the end of the ramp is the ground state of the anti-ferromagnetic Ising model $|\phi_{+}\rangle = (|\uparrow, \downarrow\rangle + |\downarrow, \uparrow\rangle)/\sqrt{2}$. **Right panel:** Incoherent case with dephasing rate $\gamma/\hbar = 0.01$ {MHz}

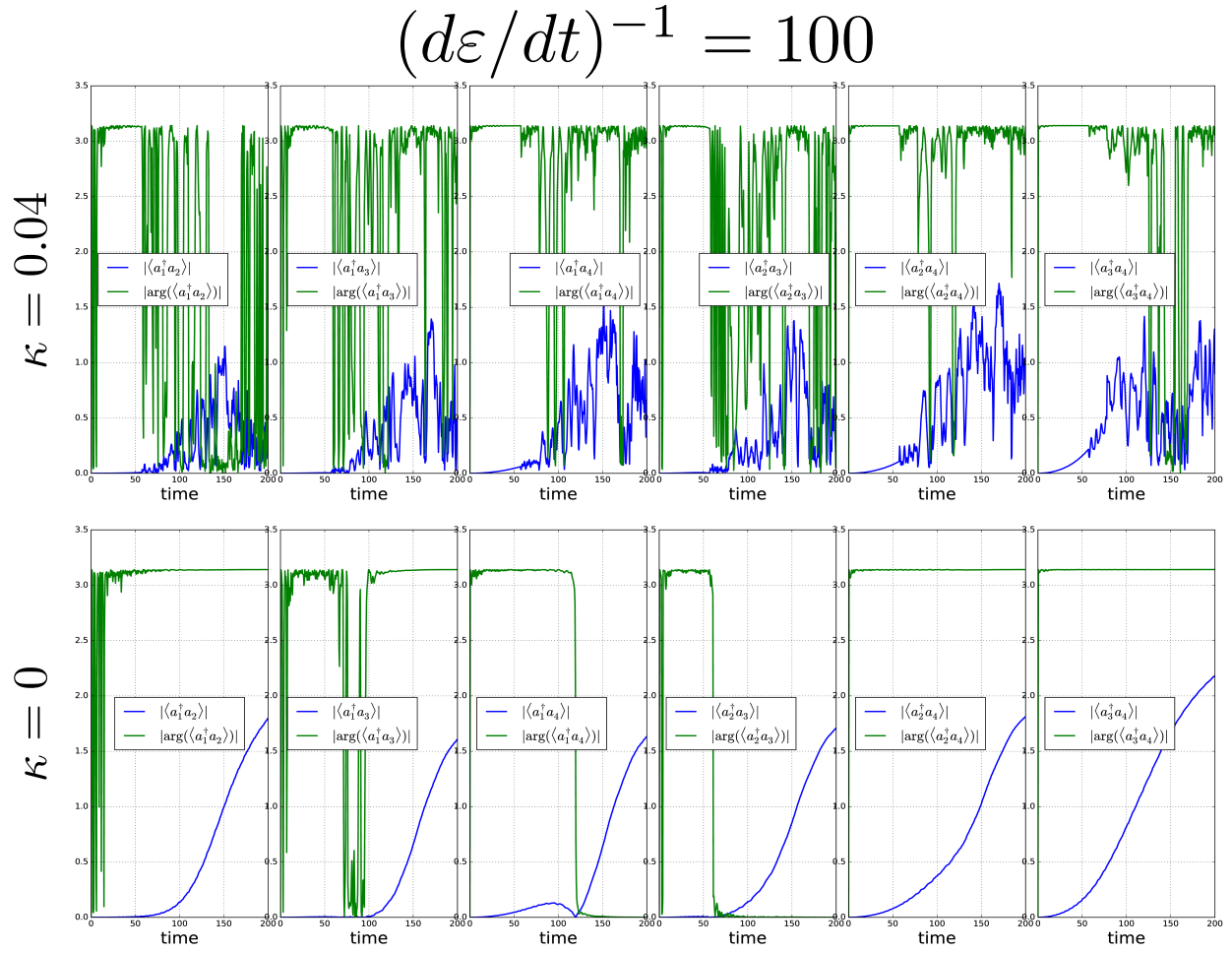
IV. TYPICAL QUANTUM TRAJECTORIES FOR THE NUMBER PARTITIONING PROBLEM

In Fig. 4 (a) of the main text, we show the success probability of the quantum Ising machine for the number partitioning with the set $S = \{4, 5, 6, 7\}$. Figs. 7, 8 and 9 show the inter-oscillator phase-correlations $\langle \mathbf{a}_n^\dagger \mathbf{a}_m \rangle$, along typical quantum trajectories corresponding to different points in Fig. 4 (a) in the main text. For two elements n and m in the same partition, the correlation is ideally π while it is zero if they are in different partitions. Explicitly, the correct solution to the considered partitioning problem has the following correlations above threshold

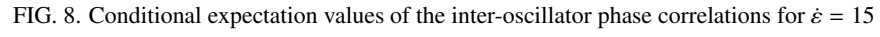
$$|\arg(\langle \mathbf{a}_1^\dagger \mathbf{a}_2 \rangle)| = |\arg(\langle \mathbf{a}_1^\dagger \mathbf{a}_3 \rangle)| = |\arg(\langle \mathbf{a}_2^\dagger \mathbf{a}_4 \rangle)| = |\arg(\langle \mathbf{a}_3^\dagger \mathbf{a}_4 \rangle)| = \pi \quad (76)$$

$$|\arg(\langle \mathbf{a}_2^\dagger \mathbf{a}_3 \rangle)| = |\arg(\langle \mathbf{a}_1^\dagger \mathbf{a}_4 \rangle)| = 0. \quad (77)$$

Note that the phases only have meaning when $\langle \mathbf{a}_n^\dagger \mathbf{a}_m \rangle \neq 0$. Clearly, we see by comparing Figs. 7, 8 and 9 with Fig. 4 (a) of the main text, that for parameter values corresponding to the blue region in Fig. 4 (a), the typical trajectories display the correct correlations, while for parameters in the red regions, the correlations do typically not all have the correct values at the end of the ramp. We also see that in regions with higher number of photon loss events, the noise in the conditional expectation values increases. For example, the trajectories at $\kappa = 0$ and $\kappa = 0.04$ for $\varepsilon = 3$, in Fig. 9 are similar to each other. This corresponds to the regime of low average number of photon jumps. In contrast, the



trajectories with $\kappa = 0$ and $\kappa = 0.04$ for $\varepsilon = 100$, in Fig. 7, are markedly different. This corresponds to a regime with a higher average number of photon jumps (see Fig.4 (b) in the main text).



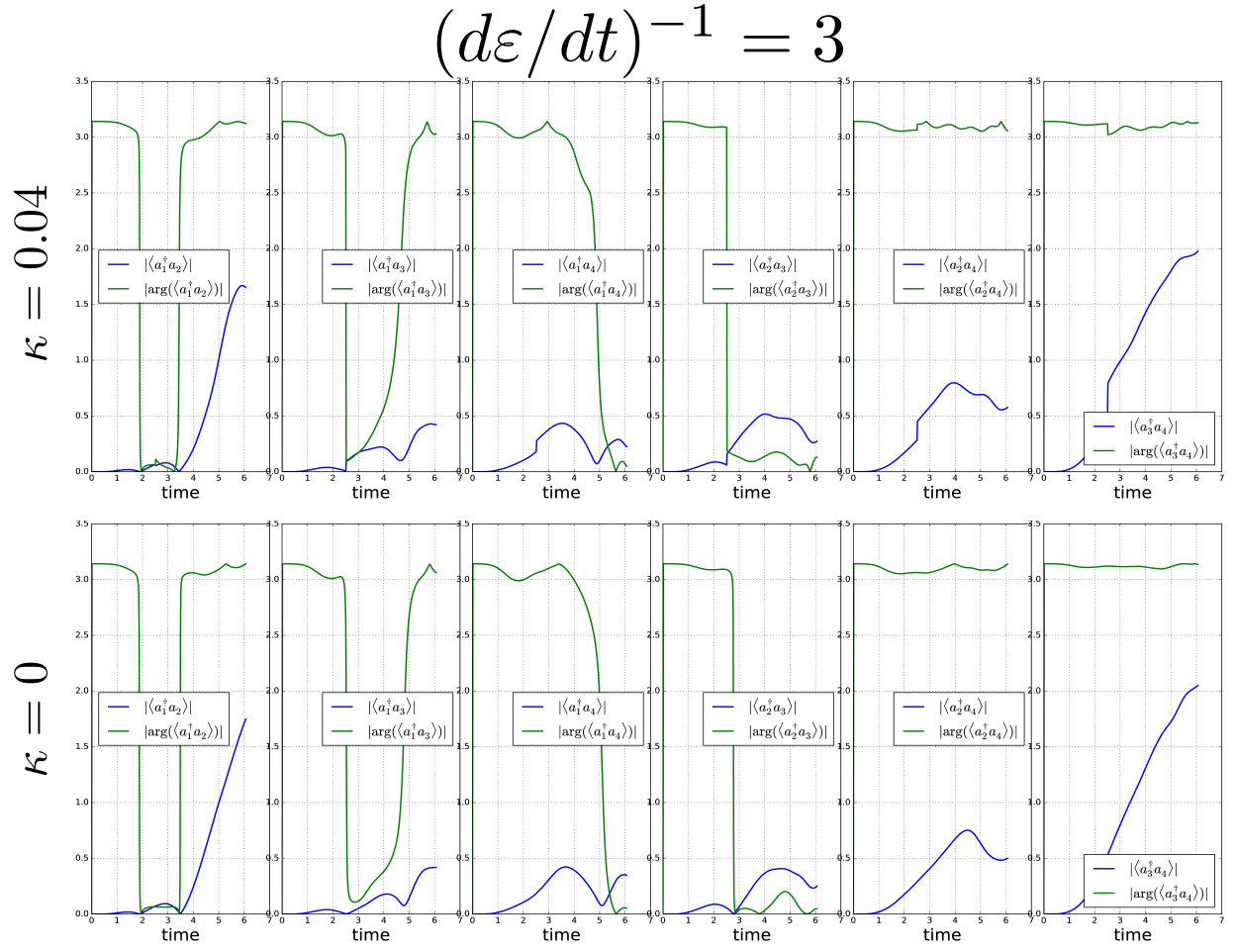


FIG. 9. Conditional expectation values of the inter-oscillator phase correlations for $\varepsilon = 3$

-
- ¹ T. Yamamoto, K. Inomata, M. Watanabe, K. Matsuba, T. Miyazaki, W. D. Oliver, Y. Nakamura, and J. S. Tsai, *Applied Physics Letters* **93**, 042510 (2008).
 - ² W. Wustmann and V. Shumeiko, *Phys. Rev. B* **87**, 184501 (2013).
 - ³ J. Koch, T. M. Yu, J. Gambetta, A. A. Houck, D. I. Schuster, J. Majer, A. Blais, M. H. Devoret, S. M. Girvin, and R. J. Schoelkopf, *Phys. Rev. A* **76**, 042319 (2007).
 - ⁴ D. F. Walls and G. J. Milburn, *Quantum optics* (Springer, 2008), 2nd ed.
 - ⁵ M. V. Berry and M. Wilkinson, *Proc. R. Soc. Lond.* **392**, 15 (1984).
 - ⁶ G. Vidal and R. F. Werner, *Phys. Rev. A* **65**, 032314 (2002).
 - ⁷ M. H. Michael, M. Silveri, R. T. Brierley, V. V. Albert, J. Salmilehto, L. Jiang, and S. M. Girvin, *Phys. Rev. X* **6**, 031006 (2016).
 - ⁸ N. Ofek, A. Petrenko, R. Heeres, P. Reinhold, Z. Leghtas, B. Vlastakis, Y. Liu, L. Frunzio, S. M. Girvin, L. Jiang, et al., *Nature* **536**, 441 (2016), letter.
 - ⁹ M. Mirrahimi, Z. Leghtas, V. V. Albert, S. Touzard, R. J. Schoelkopf, L. Jiang, and M. H. Devoret, *New Journal of Physics* **16**, 045014 (2014).
 - ¹⁰ S. Puri and A. Blais, arXiv:1605.09408 (2016).